ON THE ONSET OF CENTRAL ATLANTIC MAGMATIC PROVINCE (CAMP) VOLCANISM AND ENVIRONMENTAL AND CARBON-CYCLE CHANGE AT THE TRIASSIC–JURASSIC TRANSITION (NEUQUÉN BASIN, ARGENTINA)

Ruhl, M.[1,2,], Hesselbo, S.P.[3], Al-Suwaidi, A.[4], Jenkyns, H.C.[2], Damborenea, S.E.[5], Manceñido, M.O.[5], Storm, M. [2,6], Mather, T.A.[2], Riccardi, A.C.[5]*

[1] Department of Geology, Trinity College Dublin, The University of Dublin, College Green, Dublin 2, Dublin, Ireland
[2] Department of Earth Sciences, University of Oxford, South Park Road, OX1 3AN, Oxford, UK
[3] Camborne School of Mines and Environment and Sustainability Institute, University of Exeter, Penryn TR10 9FE, UK
[4] Department of Earth Sciences, Khalifa University of Science and Technology, PO Box 127788, Abu Dhabi, United Arab Emirates
[5] Departamento Paleontología Invertebrados, Museo de Ciencias Naturales La Plata, Paseo del Bosque s/n, 1900 La Plata, Argentina
[6] Department of Earth Sciences, Stellenbosch University, Stellenbosch 7600, South Africa
* Corresponding author's email-address: micha.ruhl@tcd.ie

ABSTRACT

The Triassic–Jurassic transition is characterized by the end-Triassic mass extinction approximately synchronous with the onset of emplacement of the Central Atlantic Magmatic Province (CAMP), and associated with a major negative carbon-isotope excursion (CIE) affecting the ocean–atmosphere system. Here, we present new data (total organic carbon, pyrolysis analysis, carbon-isotopes from bulk organic matter, elemental mercury, and other elemental contents) from a southern-hemisphere Triassic–Jurassic boundary succession in the Neuquén Basin, Argentina. The end-Triassic mass extinction there coincides with a relatively small (2–3‰) negative CIE in bulk organic matter, and we present a model that suggests that extreme aridity across the western Pangaean landmass may have resulted in rather limited terrestrial organic-matter flux to the sedimentary realm in eastern

Panthalassic marine basins, hypothetically reducing the magnitude of the observed negative CIE in $\delta^{13}C_{TOC}$.

Increased deposition of sedimentary Hg (and Hg/TOC and Hg/Zr) in the marine Neuquén Basin began stratigraphically before the negative CIE associated with the end-Triassic mass extinction, and thus before the commencement, in North America and Africa, of CAMP-related basaltic volcanism, but possibly coinciding with the early emplacement of CAMP-associated intrusives (dykes and sills). This relative chronology suggests thermal alteration of intruded country rocks and/or intrusive magmatic degassing of Hg as potential major sources of elevated Hg fluxes to the atmosphere at this time.

The Neuquén Basin experienced the development of dysoxic–anoxic marine conditions across the Triassic–Jurassic transition, enabling increased preservation of organic matter. Simple mass-balance calculations show that enhanced carbon burial rates can explain the inferred evolution of the global exogenic carbon cycle across this time-interval.

Keywords: Carbon-cycle change, Triassic–Jurassic mass extinction, CAMP volcanism, palaeo-climate change, mercury (Hg), anoxia

[1] INTRODUCTION

Central Atlantic Magmatic Province (CAMP) volcanism and the associated release of greenhouse gases and toxic compounds has been suggested as the initiator of or driver for major climatic and environmental perturbations at the Triassic–Jurassic transition (e.g. Marzoli et al., 2004; van de Schootbrugge et al., 2009; Deenen et al., 2010; Panfili et al., 2019). The release of carbon into the ocean-atmosphere system likely led to significantly elevated atmospheric pCO_2 levels (McElwain et al., 1999; Bonis et al., 2010; Schaller et al., 2011; Steinthorsdottir et al., 2011; Schaller et al., 2012; Schaller et al., 2015) and an associated increase in

60 global temperatures in the oceans and atmosphere (Korte et al., 2009; McElwain et
61 al., 1999; Ruhl et al., 2010; Bonis and Kürschner, 2012). The climatic and
62 environmental repercussions of Triassic–Jurassic carbon release are suggested to
63 have led to the end-Triassic mass extinction in the marine realm, with the loss of
64 most ammonoid and all conodont species and major extinctions in many other
65 marine invertebrate groups (e.g. Mander et al., 2008; Mander and Twitchett, 2008;
66 Hillebrandt et al., 2013, and references therein). Terrestrial ecosystems were also
67 severely affected, with major changes in vegetation (e.g. van de Schootbrugge et al.,
68 2009; Mander et al., 2010; Bonis and Kürschner, 2012). The principle processes
69 leading to marine extinctions probably varied geographically, through time, and
70 between faunal groups, but enhanced atmospheric pCO_2 levels likely led to the
71 Triassic–Jurassic transition being one of the strongest ocean acidification events of
72 the Phanerozoic Eon (Črne et al., 2011; Greene et al., 2012; Hönisch et al., 2012;
73 Ikeda et al., 2015).
74 Carbon release from the lithosphere to the atmosphere and ocean, associated
75 with CAMP magmatism, and the possible initiation of positive and negative feedback
76 mechanisms in the global carbon-cycle, also resulted in major changes in global
77 (bio)geochemical cycling, manifested as a series of negative and positive excursions
78 in organic and inorganic marine and terrestrial carbon-isotope records. The release
79 of ^{13}C-depleted carbon from CAMP volcanogenic degassing, possibly combined with
80 the release of bio- and thermogenic ^{13}C-depleted carbon from the dissociation of
81 seafloor methane clathrates and thermally altered subsurface organic-rich shales
82 intruded by dykes and sills, likely contributed to or caused the observed negative
83 carbon-isotope excursion (CIE) coincident with the end-Triassic mass extinction
84 (Hesselbo et al., 2002; Ruhl et al., 2009; Ruhl et al., 2011). The magnitude of this
85 negative CIE is poorly constrained and varies between 1 and 8‰ in marine and
86 continental (terrestrial and lacustrine) organic and inorganic bulk-rock and molecular
87 biomarker archives (Pálfy et al., 2001; Hesselbo et al., 2002; Galli et al., 2005; van

de Schootbrugge et al., 2008; Korte et al., 2009; Ruhl et al., 2009; Deenen et al., 2010; Ruhl et al., 2010; Whiteside et al., 2010; Črne et al., 2011; Deenen et al., 2011; Ruhl et al., 2011; Bartolini et al., 2012; Lindström et al., 2012; Dal Corso et al., 2014; Al-Suwaidi et al., 2016; Yager et al., 2017). The uncertainty in the size of the observed CIE and thus the associated carbon-cycle change at this time severely hampers mass-balance constraints on the magnitude and rate of carbon release associated with the onset of CAMP emplacement, and related carbon release from e.g. ocean-floor methane hydrate reservoirs or intruded subsurface organic-rich shales, and the associated changes in the fluxes of carbon between the exogenic carbon reservoirs.

Here, determinations of newly collected ammonites, bivalves and brachiopods have allowed improved stratigraphic resolution of an expanded Triassic–Jurassic boundary section in the Neuquén Basin, Argentina, and are accompanied by new $\delta^{13}C_{TOC}$, Hg (and Hg/TOC and Hg/Zr) and elemental concentration data. We show that the magnitude of the observed negative CIE over the interval of the end-Triassic mass extinction varies geographically, with only minor 2–3‰ negative excursions in bulk $\delta^{13}C_{TOC}$ observed in marine basins along the western Pangaean continental margin, bordering the eastern Panthalassic Ocean (Figure 1). This magnitude change is broadly similar to the 2–4‰ negative CIEs in bulk $\delta^{13}C_{TOC}$ observed in North American and Moroccan continental sections, but it is significantly smaller than the 4–6.5‰ negative CIEs observed in bulk $\delta^{13}C_{TOC}$ records from the Laurasian Seaway (Figure 1). We hence here provide a stratigraphic framework for the onset of CAMP magmatic activity and discuss associated environmental consequences with implications for the end-Triassic mass extinction and the magnitude of the associated end-Triassic carbon-cycle perturbation.

[2] PALAEOGEOGRAPHY, GEOLOGICAL SETTING AND SEDIMENTARY DEPOSITIONAL ENVIRONMENT

116 The Neuquén Basin is located in west central Argentina, on the eastern side of
117 the Andes, between 34° and 41° S and covers an area of about 120,000 km^2 (Figure
118 1; Supplementary Figure 1; Howell et al., 2005). The basin has a complicated
119 tectonic history associated with the break-up of Gondwana, subduction of the proto-
120 Pacific plate and the development of the Andean magmatic arc (Vergani et al., 1995,
121 and references therein). It began as a rift basin during Late Triassic to Early Jurassic
122 times and its tectonic evolution was characterized by about 220 Myr of Mesozoic–
123 Cenozoic subsidence (Vergani et al., 1995; Bechis et al., 2010, and references
124 therein). Initial rifting in the Triassic was driven by extensional collapse of a Permo–
125 Triassic orogenic belt and early syn-rift sequences were restricted to isolated
126 depocentres limited by normal faults (Vergani et al., 1995). The location and
127 geographical extent of the main depocentre evolved significantly through the
128 Jurassic, associated with changes in accommodation space and sediment supply in
129 response to eustatic sea-level change and tectonic processes (Vicente, 2005;
130 Vicente, 2006; Lanés et al., 2008; Riccardi et al., 2011). From the Aalenian (Middle
131 Jurassic) onward, fault-controlled subsidence was replaced by regional subsidence,
132 but several episodes of structural inversion modified the shape of the depocentre and
133 rejuvenated sedimentary source areas. The tectonic evolution of the basin is
134 reflected in a complex structural and depositional framework, and resulted in the
135 formation of several major hydrocarbon source-rock intervals, and numerous
136 reservoir zones (Vergani et al., 1995).
137 The north–south oriented Neuquén Basin contains up to 6 km of Triassic to
138 Cenozoic sediments in its most central part, which accumulated in several
139 depositional cycles representing a pre-rift phase through to foreland-basin
140 development (Howell et al., 2005). The sedimentary succession of the Atuel
141 depocentre studied here is situated in the northern Andean sector of the northern
142 Neuquén Basin (Supplementary Figure 1) and formed in the Late Triassic (Norian),

143 with marine sedimentary infill recording the first stages of the basin opening as a rift
144 system (Bechis et al., 2010, and references therein).
145 The Triassic to Jurassic infill of the Atuel depocentre consists of siliciclastic
146 marine and continental sediments of the Arroyo Malo, El Freno, Puesto Araya and
147 Tres Esquinas Formations (Riccardi et al., 1991; Lanés, 2005; Lanés et al., 2008;
148 Bechis et al., 2010). Accommodation space *vs* sediment supply varied through time,
149 with syn-rift depositional conditions occurring from Rhaetian to late Early Sinemurian
150 times (marked by accommodation space >> sediment supply; Lanés, 2005). At this
151 time sediments were deposited in slope-type fan deltas in the west, and coeval
152 braided fluvial systems in the east (Lanés, 2005; Lanés et al., 2008), while active
153 normal faults controlled the palaeogeography and lateral variations of the
154 depositional systems (Bechis et al., 2010).
155 The Early Jurassic syn-rift deposition gave way to a sag phase in Sinemurian–
156 Toarcian times, with accommodation space exceeding sediment supply, allowing for
157 a marked increase in the marine depositional area, a transgression of the marine
158 shelf and a deepening of the depositional environment. Marine syn-rift sediments are
159 up to ~980 m thick in the western part of the Atuel depocentre, with continental
160 deposits forming, thinning out and disappearing towards the east (Bechis et al.,
161 2010). In the Neogene, the Andean orogeny deformed and uplifted the depocentre
162 infill, leading to exhumation of the syn-rift deposits and their exposure in the northern
163 sector of the Malargüe fold and thrust belt (Bechis et al., 2010, and references
164 therein).
165 The Upper Triassic and Lower Jurassic marine sediments of the Arroyo Malo
166 Formation are interpreted as mainly consisting of fan-delta facies with planar
167 laminated mudstones, fine sandstones and conglomeratic lenses deposited by low-
168 and high-density turbidity currents and debris flows (Lanés, 2005; Lanés et al.,
169 2008). Sediments may have entered the Neuquén Basin from two main source
170 areas: the Chilean Coastal Cordillera that supplied immature volcaniclastic material

and cratonic areas to the east that introduced more mature material (Tunik et al., 2008).

[3] MATERIALS & METHODS

The Triassic–Jurassic marine sedimentary succession at Arroyo Alumbre is remotely located in the Andes mountains, west of the main road from Malargüe to Mendoza (leaving the main road at El Sosneado), at 34°49'767''S – 69°53'224''W (Google-maps coordinates: -34.827675 (South), -69.888884 (West)) (Supplementary Materials and Supplementary Materials Figures 2 A–E). The section was sampled during two field seasons (2014 and 2016). The Arroyo Alumbre (and associated nearby Arroyo Malo) sections were previously studied and described by Riccardi et al. (1988, 1997, 2004), Lanés (2005), Lanés et al. (2008), Damborenea and Manceñido (2012), and Damborenea et al. (2017), who distinguished the Arroyo Malo Formation at the base (0–280 m), followed by the conglomeratic lenses of the El Freno Formation and the stratigraphically higher deposits of the El Cholo Formation. The Triassic–Jurassic sediments of the Arroyo Alumbre/ Arroyo Malo section were deposited in the northern sector of the Neuquén Basin, in the Atuel depocentre (Lanés, 2005; Lanés et al., 2008; Bechis et al., 2010; Damborenea et al., 2017). The Triassic–Jurassic samples geochemically studied here are from ~124–271 m in the Arroyo Alumbre section, and all come from the Arroyo Malo Formation (Figure 2). The Triassic–Jurassic sedimentary succession at Arroyo Alumbre is characterized by the monotonous occurrence of dark-coloured shales and mudstones, apart from sporadic turbiditic or debris flow beds (1–10cm thick; consisting of fine-grained sands to coarse-grained silts). The rare gravity flows were avoided when sampling of the studied stratigraphic section, with collected samples all consisting of shales and mudstones (Supplementary Figure 2 D–E). The monotonous dominant lithology in the samples collected, is exemplified by relatively unchanging sedimentary zirconium (Zr) concentrations (Figure 2).

Ammonite, bivalve and brachiopod samples were collected for biostratigraphical constraints and published in Damborenea et al. (2017) and Riccardi (2019). Bulk samples were collected and analysed for chemostratigraphy ($\delta^{13}C_{TOC}$), organic carbon and pyrolysis (Rock-Eval) analyses, mercury analyses (suggested previously to reconstruct CAMP-activity; Percival et al., 2017), and elemental/ palaeoenvironmental study (Hand-Held X-Ray Fluorescence (hh-XRF)). Detailed description of methods is provided in the on-line Supplementary Information section.

[4] RESULTS & DISCUSSION

[4.1] INTEGRATED BIO- & CHEMOSTRATIGRAPHY OF THE TRIASSIC–JURASSIC TRANSITION AT ARROYO ALUMBRE/ ARROYO MALO

The studied Triassic–Jurassic succession at Arroyo Alumbre/ Arroyo Malo (Neuquén Basin, Argentina) contains relatively diverse marine invertebrate macrofossils, such as ammonites, bivalves and brachiopods (Figure 2 and 3; Riccardi et al., 2004; Damborenea and Manceñido, 2012 and references therein; Damborenea et al., 2017; Riccardi, 2019).

The presence of marine Triassic strata in Argentina was initially proposed on the basis of bivalves and brachiopods found in marine deposits near Cerro Chachil and near Piedra del Águila (both in the Neuquén Province; Groeber, 1924, 1929; Groeber et al., 1953). These fossils, however, were later recognized as Early Jurassic in age (Leanza, 1948; Frenguelli, 1948; Leanza, 1992; Manceñido and Leanza, 1993; Pérez et al., 1995). Upper Triassic (Norian and/or Rhaetian) marine fossils (mollusc and brachiopod faunas) were subsequently reported from Arroyo Malo, in the river Atuel area of the Southern Mendoza province, in deposits below the lower Hettangian sediments that had a fauna pertaining to the *Psiloceras rectocostatum* Zone (Riccardi et al., 1991; Riccardi et al., 1997; Riccardi et al., 2004; Riccardi, 2008; Manceñido, 2002; Damborenea and Manceñido, 2012; Riccardi,

2019). A late Rhaetian age for these deposits was confirmed by the occurrence of *Choristoceras* cf. *marshi* (Riccardi and Iglesia Llanos, 1999; Riccardi, 2008, 2019). Upper Triassic and Lower Jurassic marine faunas described for the Arroyo Malo/ Arroyo Alumbre sections were found throughout the succession (Figure 2; Damborenea & Manceñido, 2012; Damborenea et al., 2017; Riccardi, 2019). Bivalves are the most numerous and diverse group, with at least 15 species (and almost as many families; Damborenea and Manceñido, 2012; Damborenea et al., 2017). Apart from the bivalves and brachiopods, this fauna also includes Triassic and Jurassic ammonoids, three gastropod species, a cnidarian, and some microfossils (foraminifers and ostracods) (Damborenea and Manceñido, 2012). A few impressions of plant remains are also present (suggested to be of *Zuberia* and Equisetales affinity amongst others (Riccardi et al., 1997, 2004; Damborenea and Manceñido, 2012).

New ammonite finds were recently described in Riccardi (2019), as part of a wider review of cephalopod fossils from this section. Triassic cephalopods were found *in situ* in the lower part of the section (at 2–73 m), including the heteromorph ammonoids *Rhabdoceras suessi*, *?Peripleurites* and the coleoid *Aulacoceras cf. carlottense*, suggesting a late Norian age. An *ex situ* specimen of the latest Rhaetian *Choristoceras marshi* was found at ~135 m in the section (Riccardi, 2019). Given the steep nature of the outcrop, and the non-overturned nature of the bedding, this specimen likely originated from this level or from higher up the succession; this is consistent with the *in situ* occurrence of Rhaetian nannofossils up to ~10m above this level (Angelozzi personal communication).

The *ex situ* find of the earliest Jurassic ammonite *Psiloceras tilmanni* at ~176 m suggests the occurrence of the *tilmanni* Subzone of the *tilmanni* Zone stratigraphically at or above this level. The *in situ* record of *Psiloceras* cf. *primocostatum* and *P.* cf. *polymorphum*, and the *ex situ* record of *P.* cf. *pressum* between 188–197 m are indicative of the *planocostatum* Subzone of the *tilmanni*

255 Zone, and/or the *primocostatum* Zone of the Andean zonation (or the *polymorphum*
256 Zone in the North American zonation; Guex, 1995). The *in situ* record of *Psiloceras*
257 *rectocostatum* at ~230 m in the section indicates the *rectocostatum* Zone. The
258 Andean *primocostatum* and *rectocostatum* (and the North American *polymorphum*)
259 zones all temporally overlap with the European *planorbis* Zone (Riccardi, 2008; von
260 Hillebrandt et al., 2013).

261 The $\delta^{13}C_{TOC}$ record presented here across the Triassic–Jurassic transition at
262 Arroyo Malo starts at ~124 m, extending to ~271 m (Figure 2). The observed values
263 in $\delta^{13}C_{TOC}$ vary between ~ –26.5‰ and ~ –29.2‰ and the record is marked by
264 significant and relatively abrupt ~ 1–2‰ fluctuations superimposed on
265 stratigraphically more extensive trends (Figure 2). The lowest Jurassic ammonites
266 recorded *in situ*, occur ~9 m above a distinct negative carbon-isotope excursion
267 (CIE). The position of this negative CIE, relative to the ammonite record, combined
268 with the more stratigraphically extensive trends in $\delta^{13}C_{TOC}$, is remarkably similar to
269 what is observed for other Triassic–Jurassic boundary sections, such as at St
270 Audries Bay (Bristol Channel Basin, UK) or New York Canyon (Nevada, USA)
271 (Figure 3; Hesselbo et al., 2002; Hesselbo et al., 2004; Bartolini et al., 2012). The
272 record at Arroyo Malo is, however, 4–5 times more expanded compared to St
273 Audries Bay and the changes in magnitude of $\delta^{13}C_{TOC}$ are generally smaller. The
274 integrated bio- and chemostratigraphical framework for the Arroyo Malo section
275 presented here allows for direct high-resolution correlation with Triassic–Jurassic
276 records elsewhere (Figure 3).

277

278 **[4.2] CAMP MAGMATISM RECORDED IN THE NEUQUÉN BASIN (ARGENTINA)**

279 Mercury (Hg) analyses are increasingly being used to constrain the
280 stratigraphical occurrence of large igneous province (LIP) volcanism in the
281 Phanerozoic history of the planet (Percival et al., 2018 and references therein).
282 Gaseous mercury has a relatively short residence time in the present-day

283 atmosphere, of 0.5–2 years (Schroeder and Munthe, 1998; Blum et al., 2014; Pyle
284 and Mather, 2003). The element can be sequestered into marine and terrestrial
285 sediments through several pathways, but a major route into the sedimentary realm is
286 after uptake by and deposition with organic matter (for which reason sedimentary Hg
287 concentrations are commonly normalized against the sedimentary total organic
288 carbon concentration (Hg/TOC)). Despite its promise, numerous important questions
289 remain to be answered before Hg can be claimed as an unequivocal fingerprint of
290 LIP volcanism, as well as an understanding of why some sedimentary records
291 document clear Hg enrichment signals whilst others do not. Of particular importance
292 is evaluating the impact of different volcanic styles on the global mercury cycle, as
293 well as the role played by depositional processes in recording global Hg-cycle
294 perturbations (Percival et al., 2018 and references therein).
295 Nevertheless, evidence from multiple sections suggests that Central Atlantic
296 Magmatic Province volcanism likely had a major impact on the global mercury cycle,
297 and relatively elevated sedimentary Hg and Hg/TOC values are reported from
298 geographically widespread continental and marine sedimentary basins in the USA
299 (Nevada), Canada (Partridge Island), East Greenland (Jameson Land), Austria
300 (Eiberg Basin), the UK (Bristol Channel Basin), and Morocco (Argana Basin) (Figure
301 1; Thibodeau et al., 2016; Percival et al., 2017). Accumulation of enhanced
302 sedimentary Hg at the Triassic–Jurassic transition appears to have begun close to
303 the time of the end-Triassic mass extinction, contemporaneously with the initial
304 emplacement of CAMP basalts in the Argana Basin and the High Atlas Mountains
305 (Morocco). Subsequent uppermost Triassic and Lower Jurassic peaks in mercury
306 levels appear to be pulsed, and are possibly aligned, age-wise, with the major CAMP
307 basalt flows as reported from North America and Morocco (Percival et al., 2017).
308 Mercury (Hg) analyses on the expanded Upper Triassic to Lower Jurassic
309 Arroyo Alumbre sedimentary succession in the Neuquén Basin show a relative
310 increase in Hg concentrations from on average ~10 ppb below ~169m in the studied

311 section, increasing up to ~60 ppb at ~189 m (Figure 2). As stated above, Hg
312 drawdown into marine sediments can be controlled by variations in the organic-
313 matter flux to the sediment-water interface; sedimentary Hg concentrations are
314 therefore commonly normalized against TOC (Percival et al., 2015). Also Hg/TOC
315 values in the studied succession (in samples with TOC > 0.25%; lower TOC values
316 are impacted by increasingly large analytical uncertainties) increase from ~169m
317 upward, suggesting an increased Hg-flux to the sediment-water interface,
318 independent of sedimentary organic-matter enrichment (Figure 2).
319 Sedimentary Hg concentrations could alternatively have resulted from
320 changes in the depositional environment and associated changes in sediments
321 supplied, and the rate of sedimentation. However, all studied samples represent a
322 monotonous shale or mudstone lithology, void of major stratigraphic changes as
323 exemplified by relatively constant sedimentary Zr concentrations (Figure 2). A major
324 increase in Hg/Zr values, onsetting at ~169 m in the studied succession, therefore
325 suggests that lithology plays no major role in the stratigraphical evolution of
326 sedimentary Hg concentrations (Figure 2). The data-set presented here suggests
327 that elevated sedimentary Hg (and Hg/TOC & Hg/Zr) values initiated before the
328 negative CIE associated with the end-Triassic mass extinction (Figure 2).
329 Mercury in the present day not only released from volcanogenic degassing on
330 land or along mid-ocean ridges (Pyle and Mather, 2003; Bowman et al., 2015), but
331 also by the thermogenic alteration of subsurface organic-rich deposits (O'Keefe et
332 al., 2010). CAMP-associated dykes and sills intruded sedimentary basins in South
333 America and western Africa up to 100 kyr predating the earliest known age of CAMP
334 basaltic extrusion (Davies et al., 2017; Heimdal et al., 2018). Hence, elevated Hg
335 loading (leading to increased sedimentary Hg, Hg/TOC and Hg/Zr levels) at a time
336 apparently before the negative CIE associated with the end-Triassic mass extinction,
337 may suggest that mercury was not only released into the atmosphere through direct
338 volcanogenic degassing, but possibly also expelled via intrusions of CAMP-

339 associated dykes and sills into subsurface organic-rich shales (Figures 2 and 6;
340 Percival et al., 2015; Jones et al., 2019). Volcanic Hg measurements from fumaroles
341 and diffuse soil emissions associated with CO_2 (rather than SO_2) degassing (e.g.,
342 Bagnato et al., 2014) also suggest that some degree of magmatic Hg degassing
343 within the crust, associated with intrusive (rather than purely extrusive) magmatism,
344 may also play a role.
345 Observed peak Hg and Hg/TOC values of ~50 ppb and ~150 ppb/%,
346 respectively, in Arroyo Alumbre are, however, lower than those observed in
347 contemporaneous sediments from New York Canyon and Greenland (Figure 1;
348 Thibodeau et al., 2016; Percival et al., 2017), which might reflect (I) higher sediment
349 accumulation rates (albeit without a significant lithological change) in the Neuquén
350 Basin at the time (and associated dilution of the Hg signal), (II) a relatively small
351 contribution of terrestrially sourced organic matter to the basin, with an associated
352 lower Hg-shuttling capacity (Them et al., 2017), and/or (III) the geographically closer
353 and/or downwind position of the Greenland and New York Canyon localities relative
354 to CAMP igneous centres (Figure 1).
355
356 **[4.3] MAGNITUDE OF THE END-TRIASSIC CARBON-CYCLE PERTURBATION**
357 The observed negative carbon-isotope excursion (CIE) at the end-Triassic
358 mass extinction directly predated the onset of CAMP basalt eruptive flows in the
359 Fundy, Newark and Hartford Basins (North America; Cirilli et al., 2009; Whiteside et
360 al., 2010), but coincided with the onset of CAMP basalt emplacement in the Argana
361 Basin and High Atlas Mountains (Morocco; Deenen et al., 2010; Dal Corso et al.,
362 2014; see also a review by Korte et al., 2019 and references therein; Panfili et al.,
363 2019). The onset of eruption of the major CAMP basalt flows at the time of the end-
364 Triassic mass extinction was, however, likely preceded by intrusions of major dykes
365 and sills, feeding the oldest basalt extrusives, up to ~100 kyr earlier (Marzoli et al.,
366 2011; Dal Corso et al., 2014; Davies et al., 2017; Panfili et al., 2019).

367 Carbon-cycle evolution during the end-Triassic mass extinction and across the
368 Triassic–Jurassic transition has in recent years been intensely studied in marginal
369 marine and continental basins across Asia, northern Africa, Europe and North and
370 South America (see Schobben et al., 2019 and references therein). The magnitude
371 of the $\delta^{13}C_{TOC}$ negative CIE at the level of the end-Triassic mass extinction generally
372 varies between -4 and -6.5‰ in European marine basins. Carbon-isotope records of
373 marine skeletal material ($\delta^{13}C_{Calcite}$) do not exist across the whole span of this time-
374 interval, possibly partly due to extinction and/or reduced preservation of calcite-
375 secreting organisms under low *p*H conditions (Črne et al., 2011; Greene et al., 2012;
376 Hönisch et al., 2012; Ikeda et al., 2015). Many bulk carbonate carbon-isotope
377 ($\delta^{13}C_{CARB}$) records across Europe and the north-western Tethys, however, show only
378 a much smaller 1–3‰ negative CIE (Clémence et al., 2010; Črne et al., 2011; Korte
379 and Kozur, 2011; Felber et al., 2015). Similarly, bulk carbonate carbon-isotope
380 ($\delta^{13}C_{CARB}$) records in the eastern Tethys (Tibet and the Qiangtang Basin, China)
381 show a 1.5–4‰ negative shift (Yin et al., 2006; Hu et al., 2020). Some $\delta^{13}C_{CARB}$
382 records, however, show a much larger negative shift, of 6–8‰, at the level of the
383 end-Triassic mass extinction, but these localities are notably marked by the effects of
384 diagenetic carbonate precipitation and/or cementation (central and northern Italy:
385 Bachan et al. (2012), Bachan and Payne (2015); Doniford, Somerset, UK: Clémence
386 et al. (2010)), and/or carbonate deposition in a relatively restricted basin (such as
387 recorded in the Csővár section, Hungary; Pálfy et al., 2001), and/or carbonate
388 deposition in a local calcium-rich lagoonal setting (such as the Wadi Milaha and Wadi
389 Niqab sections of the United Arab Emirates; Al-Suwaidi et al., 2016; Ge et al., 2018).
390 Interestingly, the latter two sections in the United Arab Emirates, as well as the
391 Csővár section in Hungary only show a minor 2–3‰ negative CIE in $\delta^{13}C_{TOC}$ (Figure
392 1; Pálfy et al., 2001; Ge et al., 2018).
393 The expanded Arroyo Alumbre section studied here also shows only a minor
394 2‰ negative CIE in $\delta^{13}C_{TOC}$ across the level of the end-Triassic mass extinction

395 (Figure 2). Importantly, other successions from marine basins bordering the western
396 Pangaean continental margin (along the eastern Panthalassic Ocean; Figure 1), are
397 also marked by only a minor 2–3‰ negative CIE over this interval (Figures 1 and 4).
398 This distinct palaeogeographic disparity between the magnitude of the $\delta^{13}C_{TOC}$
399 negative CIE between the north-western Tethys Ocean and the Eastern Panthalassic
400 marine basins may give crucial clues concerning regional Triassic–Jurassic climatic
401 and environmental conditions.
402 The Triassic–Jurassic transition was possibly marked by a tripling to
403 quadrupling of atmospheric pCO_2 concentrations, based on stomatal density
404 analyses and pedogenic carbonate $\delta^{13}C$ (McElwain et al., 1999; Schaller et al., 2011,
405 2012; Steinthorsdotttir et al., 2011). Elevated and increasing atmospheric pCO_2
406 concentrations linked to CAMP-associated greenhouse gas release likely had a
407 profound impact on global climate, primarily on temperature and precipitation, with
408 significant warming and possible decreased humidity in some coastal marine regions
409 and continental interiors, respectively (Korte et al., 2009; Bonis et al., 2009; Bonis et
410 al., 2010; Ruhl et al., 2010; Bonis and Kürschner, 2012; Steinthorsdottir et al., 2012).
411 Triassic–Jurassic continental configuration, with the Pangaean supercontinent
412 spanning both hemispheres, would have affected regional climatic and environmental
413 conditions (Kent et al., 2014). This continental configuration, combined with elevated
414 atmospheric pCO_2 and average global temperatures at that time, likely prevented
415 effective penetration of humidity and precipitation into the vast continental interior,
416 leading to strongly reduced rainfall (and elevated evaporation over precipitation
417 rates) across the central and western Pangaean landmass (Figure 1; Chandler et al.,
418 1992; Huynh and Poulsen, 2005). Extremely warm and dry conditions likely affected
419 western Pangaean continental interiors between the latitudes of 60º north and south
420 (Chandler et al., 1992; Huynh and Poulsen, 2005), possibly in response to poleward
421 expansion of the Hadley cells and associated subtropical climate belts (Figure 1), as

422 also predicted by models for anthropogenic greenhouse-gas warming (Hu and Fu,
423 2007; Lu et al., 2007; Previdi and Liepert, 2007; Kang and Lu, 2012).
424 The climatic effect of the Pangaean continental configuration, combined with
425 elevated Triassic–Jurassic greenhouse conditions, may have profoundly impacted
426 the occurrence and dominant type of vegetation across the central and western part
427 of the landmass, with the mid-latitudes possibly largely characterized by desert-like
428 conditions, with very limited to no vegetation and more temperate vegetation-types
429 only occurring at higher latitudes (>60º N and S; Rees et al., 2000; Sellwood and
430 Valdes, 2006, 2008). The modelled reduced to non-existent vegetative cover across
431 central and western Pangaea would likely have affected weathering rates, sediment
432 supply, and the supply of terrestrial organic matter to marginal marine basins.
433 The atmospheric flux of humidity from the oceans into continental interiors, and
434 associated precipitation and plant growth are, however, likely to have been much
435 more common along the eastern margin of Pangaea, with wetter conditions and lush
436 vegetation along most of the north-western Tethyan realm (Rees et al., 2000; Barrón
437 et al., 2006; Sellwood and Valdes, 2006, 2008; Gómez et al., 2007; McElwain et al.,
438 2007; Bonis et al., 2009; Cirilli et al., 2009; van de Schootbrugge et al., 2009; Bonis
439 and Kürschner, 2012; Lindström et al., 2012; Pieńkowski et al., 2014; Cirilli et al.,
440 2018).
441 Osmium-isotope ratios are significantly elevated across the Triassic–Jurassic
442 transition (Cohen and Coe, 2007; Kuroda et al., 2010), reflecting a relative increase
443 in the proportion of radiogenic isotopic species, suggesting overall enhanced
444 continental chemical weathering rates through this time-interval, likely in response to
445 elevated and enhanced atmospheric pCO_2 and hypothesised accelerated
446 hydrological cycling around eastern Pangaea.
447 Marginal marine basins along the sparsely vegetated western edges of the
448 Pangaean landmass have significantly expanded sedimentary successions across
449 the Triassic–Jurassic transition, with the negative CIE at the end-Triassic mass

extinction generally expressed over a stratigraphic thickness of 4–6 metres (Figure 3; *this study*; Williford et al., 2007; Bartolini et al., 2012; Thibodeau et al., 2016; Yager et al., 2017). By contrast, and despite elevated precipitation and weathering levels, the stratigraphic thickness recording the negative CIE associated with the end-Triassic mass extinction in most of the north-western Tethyan marginal marine basins, which were surrounded by well-vegetated coastal regions and hinterlands, is much more limited and generally only 30–80cm thick in siliciclastic-dominated successions (Hesselbo et al., 2002; Ruhl et al., 2009; Lindström et al., 2012; Felber et al., 2015). This pattern suggests that, in addition to a potentially larger accommodation space in the back-arc basins of western Pangaea (or possible depositional gaps or hiatuses in European sections), vegetation cover in eastern Pangaea may have played a role in stabilizing soil profiles, controlling sediment budgets and the supply of sediments to the marine realm at that time.

The prolonged Late Triassic and Early Jurassic potential scarcity in vegetation cover across western Pangaea (Figure 1; Sellwood and Valdes, 2006; 2008) likely resulted in only limited terrestrial organic-matter supply to nearby marginal marine basins. In contrast to the Tethyan realm, sedimentary organic matter in these basins may therefore have been largely marine in origin, before, during, and after the negative CIE associated with the end-Triassic mass extinction.

Marine and terrestrial organic matter generally has a significant 4–5‰ difference in its stable carbon-isotope composition (Figure 4 and 5). This difference is exemplified by the 3–5‰ more positive Early Jurassic $\delta^{13}C$ values of long-chain (C_{31} to C_{35}) *n*-alkane molecular biomarkers from terrestrial higher plant leaf-waxes, *vs* marine/aquatic algal-sourced short-chain (C_{17} to C_{21}) *n*-alkanes (e.g. Xu et al., 2017*a*), including across the end-Triassic mass extinction interval in the Eiberg Basin, Austria (Figure 4; Ruhl et al., 2011). Mixing, or a changing relative supply, of marine and terrestrial organic matter into sediments can therefore impact the bulk organic carbon-isotope ($\delta^{13}C_{TOC}$) composition of such sediments (Suan et al., 2015).

478 Although such mixing by no means entirely explains observed perturbations in
479 $\delta^{13}C_{TOC}$ across major global change events (Xu et al., 2017*a*), it can, however, affect
480 the magnitude of such excursions (Suan et al., 2015). Triassic–Jurassic
481 palynofacies, hydrogen index (HI) and nitrogen- ($\delta^{15}N$) isotope data from marine
482 basins in the northwestern Tethys realm do indeed show significant changes in origin
483 of the sedimentary organic matter and kerogen (Bonis et al., 2009; Clémence et al.,
484 2010; Paris et al., 2010; Ruhl et al., 2010; Bonis and Kürschner, 2012; Lindström et
485 al., 2012). Hydrogen indices can unfortunately, however, not be analysed for the
486 studied sedimentary succession at Arroyo Alumbre, likely due to a high level of
487 thermal maturation of the sediments.
488 The $\delta^{13}C_{TOC}$ values of sedimentary organic matter in the most negative part of
489 the negative CIE associated with the end-Triassic mass extinction level are similar, -
490 29 to -31‰, in both the north-western Tethys and Panthalassic marginal marine
491 basins, probably reflecting predominantly marine constituents due to enhanced
492 productivity (Figure 4). The ~3‰ more positive $\delta^{13}C_{TOC}$ values of sedimentary
493 organic matter in levels pre- and postdating the negative CIE in the north-western
494 Tethys realm, relative to similar coeval stratigraphy in Panthalassic marginal marine
495 basins, likely reflects increased terrestrial–marine mixing (with a relatively larger
496 input of terrestrial organic matter; Figures 4 and 5). The possibly limited vegetation
497 cover and/or standing biomass in the western Pangaean hinterland, and the
498 therefore possibly (significantly) limited terrestrial organic-matter supply to eastern
499 Panthalassic marine basins may have resulted in limited to no source mixing in these
500 localities pre- and succeeding the negative CIE. Because of this situation, changes in
501 $\delta^{13}C_{TOC}$ of the sedimentary organic matter in eastern Panthalassic marginal marine
502 basins across the Triassic–Jurassic transition may therefore better reflect true
503 changes in the exogenic carbon cycle, in this case marked by a 2–3‰ negative
504 carbon-isotope shift, similar in magnitude to that observed in bulk marine carbonate
505 ($\delta^{13}C_{CARB}$) in the north-western and eastern Tethyan realm, and the terrestrial records

506 of North America and Morocco (Figure 1 and 4). The larger amplitude negative CIE
507 of 5–6.5‰ in the north-western Tethyan region may thus illustrate a predominantly
508 aquatic organic-matter supply to marine sediments during the negative CIE,
509 contrasted by the overall mixing of terrestrial and marine organic matter before and
510 after the CIE (Figure 5), resulting in the observed elevated magnitude of the end-
511 Triassic negative CIE in this region (Figure 4).

512 The carbon-isotope composition of molecular biomarkers from higher plant leaf
513 waxes ($\delta^{13}C_{n\text{-alkanes}}$) and macrofossil wood ($\delta^{13}C_{wood}$) in the continental Newark and
514 Hartford basins also shows only a modest ~3 and 4‰ negative CIE, respectively,
515 concomitant with the end-Triassic mass extinction (Whiteside et al., 2010). Similar
516 data from coeval sediments in the Eiberg Basin (Austria), however, show a major 7–
517 8‰ negative CIE in terrestrially derived long- and short-chain *n*-alkanes (Figure 4;
518 Ruhl et al., 2011). This large-amplitude excursion may then reflect either (I) changes
519 in the dominant terrestrial vegetation (as shown from palynological studies of the
520 same samples; Bonis et al., 2009), and associated differences in biological
521 fractionation for light (^{12}C) carbon, (II) increased biological fractionation for light (^{12}C)
522 carbon in response to enhanced hydrological cycling during the end-Triassic mass
523 extinction negative CIE (Ruhl et al., 2011), and/or (III) relatively increased biological
524 fractionation for light (^{12}C) carbon in terrestrial plants, in response to elevated
525 atmospheric pCO_2 following CAMP volcanism (McElwain et al., 1999).

526 Alternatively, the $\delta^{13}C_{TOC}$ record at Arroyo Alumbre may not accurately reflect
527 the magnitude of change in $\delta^{13}C$ of exogenic carbon reservoirs during the end-
528 Triassic mass extinction, due to (1) preferential degradation of the more labile and
529 ^{13}C-depleted marine organic matter from the end-Triassic mass extinction interval
530 during thermal maturation of the sediments, or (2) reduced terrestrial biological
531 fractionation for light (^{12}C) carbon in response to reduced hydrological cycling across
532 the western Pangaean landmass during the time of the end-Triassic mass extinction.
533 Although both mechanisms are not totally rejected here, they are both considered

unlikely because multiple model studies suggest that extremely arid, desert-type conditions were likely present between ~60º North and ~60º South in western Pangaea (Figure 1); consequently, meaningful vegetation cover or standing biomass may have been absent in the hinterland of the study area. The impact of terrestrial vegetation (and potentially associated differences in fractionation during thermal maturation and/or under conditions of changing hydrological cycling) on bulk sedimentary organic carbon-isotope ratios may therefore have been negligible and may not have impacted the magnitude of the observed negative CIE at the end-Triassic mass extinction interval in the Argentinian succession. The likelihood of the observed 2‰ negative CIE associated with the end-Triassic mass extinction in the Arroyo Alumbre section reflecting true global carbon-cycle change is further corroborated by the similar magnitude negative CIE observed in other sections from eastern Panthalassa marginal marine basins (Figure 1, 4 and 5).

[4.4] ENHANCED TRIASSIC–JURASSIC CARBON RELEASE AND BURIAL

Mesozoic global-change events, such as oceanic anoxic events (OAEs) are marked by the widespread development of anoxic–euxinic conditions and the associated sequestration of carbon into organic-rich black shales (Jenkyns, 2010). The massive burial of isotopically light carbon at these times led to a prolonged positive excursion in $\delta^{13}C$ in global exogenic carbon reservoirs, observed most obviously in the case of OAE 2 at the Cenomanian–Turonian boundary (at ~94 Ma) and during the Early Toarcian OAE (T-OAE) (at ~183 Ma; Jenkyns and Clayton, 1986; Jenkyns, 1988; Tsikos et al., 2004; Xu et al., 2018). The T-OAE is furthermore marked by a major negative perturbation in global $\delta^{13}C$ records superimposed on the prolonged positive carbon-isotope excursion, possibly as a result from isotopically light carbon released as methane from ocean-floor methane-clathrates (Jenkyns et al., 2002; Hermoso et al., 2009; Hermoso and Pellenard, 2014; Xu et al., 2018; Storm et al., 2020). The duration and magnitude of CIEs associated with Mesozoic

562 OAEs are ultimately controlled by the pattern of contemporaneous carbon release
563 and carbon sequestration into marine and lacustrine sediments (Jenkyns, 2010; Xu
564 et al., 2017*a*).

565 The duration of the global exogenic carbon-cycle perturbation and the
566 associated observed negative carbon-isotope excursion (CIE) in marine and
567 terrestrial sedimentary archives at the end-Triassic mass extinction is relatively short
568 (between ~20–85 kyr; Deenen et al., 2010; Schoene et al., 2010; Ruhl et al., 2010;
569 Whiteside et al., 2010; Yager et al., 2017), much shorter than the negative CIEs that
570 characterize the Permo–Triassic boundary interval, the T-OAE and the Paleocene–
571 Eocene Thermal Maximum (PETM), each of which lasted several 100 kyr (Lourens et
572 al., 2005; Shen et al., 2011; Huang and Hesselbo, 2014).

573 Triassic–Jurassic climatic and environmental change, in response to CAMP
574 emplacement and associated carbon greenhouse gas release, would have
575 significantly impacted local and regional depositional environments. Some shallow-
576 marine basins along Triassic–Jurassic continental margins witnessed a significant
577 shift to reducing water-column conditions, with even euxinic (sulphidic) conditions in
578 the photic zone (Richoz et al., 2012; Jaraula et al., 2013; Kasprak et al., 2015; Jost et
579 al., 2017). Climatic and environmental change, and an associated increase in global
580 weathering rates at this time (Cohen and Coe, 2007; see also discussion in Ruhl et
581 al., 2016), may have enhanced the supply of nutrients to marginal marine basins and
582 coastal regions, as postulated for OAEs (Jenkyns, 2010). Many Triassic–Jurassic
583 marginal marine basins are indeed characterised by increased sedimentary total
584 organic carbon (TOC) concentrations commencing around the level of the end-
585 Triassic mass extinction, possibly in response to enhanced marine primary
586 productivity and redox changes favouring enhanced preservation (Hesselbo et al.,
587 2004; Ruhl et al., 2009; Xu et al., 2017*b*).

588 The Neuquén Basin was possibly also marked by a shift towards more
589 reducing water-column conditions at that time, allowing the drawdown of redox-

590 sensitive trace metals, such as molybdenum (Mo). In oxic conditions, Mo exists as
591 soluble molybdate (MoO_4^{2-}) that adsorbs onto Mn oxides, which only slowly
592 precipitate. In sulfidic (euxinic) waters, however, molybdate dissociates into
593 thiomolybdate anions, which are rapidly reduced to highly reactive Mo(IV) sulfides
594 that precipitate out of solution, leading to sedimentary Mo enrichment (Dahl et al.,
595 2013).

596 Sedimentary Mo concentrations are largely below the hand-held-XRF detection
597 limit (of ~3 ppm) in the lower part of the studied succession (Figure 2) and Mo/Zr
598 ratios are consequently not meaningful. Higher up in the succession Mo values do,
599 however, increase up to 20 ppm in strata representing the Triassic–Jurassic
600 transition (Figure 2; Supplementary Data File). The observed sedimentary Mo values
601 are not as enriched as in euxinic shales (Dahl et al., 2013), but high Mo fluxes from
602 the water column to the sea floor may have been masked by overall high
603 sedimentation rates in the Neuquén Basin. Furthermore, sulphur (S) and S/Zr values
604 are elevated above detection limit stratigraphically above 169 m, peaking from 181–
605 188 m in the studied succession (Figure 2), the stratigraphical interval with most
606 positive $\delta^{13}C_{TOC}$ values. The monotonous nature of the studied sedimentary
607 succession suggests that the evolution of elevated S and S/Zr values are unrelated
608 to lithology; increased S and S/Zr values may rather have resulted from elevated
609 levels of sedimentary pyrite, possibly accumulating in the sediments as micron-scale
610 pyrite framboids precipitated in the water column as well as forming diagenetically
611 below the sea floor. Combined, the elevated total organic carbon (TOC), Mo and S
612 concentrations stratigraphically coinciding with the end-Triassic mass extinctions and
613 associated carbon-cycle perturbations, do suggest that the Neuquén Basin
614 developed more reducing water column conditions (Figure 2) at the same time as
615 marginal marine basins in Europe and North America.

616 Importantly, although the Triassic–Jurassic transition was marked by a
617 prolonged negative shift in the $\delta^{13}C$ of exogenic carbon reservoirs, extending over

618 the Hettangian–Early Sinemurian interval (Hesselbo et al., 2002; van de
619 Schootbrugge et al., 2005; Ruhl et al., 2010*b*; Whiteside et al., 2010; Hüsing et al.,
620 2014; Peti and Thibault, 2017; Xu et al., 2017*b*; van de Schootbrugge et al., 2019;
621 Hesselbo et al., 2020; Storm et al., 2020), the 'initial' negative CIE characterizing the
622 end-Triassic mass extinction is separated from this long-term negative shift by a
623 globally observed pronounced positive excursion in $\delta^{13}C$ (Figures 2, 3 and 6;
624 Hesselbo et al., 2002). This positive excursion in the $\delta^{13}C$ of exogenic carbon
625 reservoirs stratigraphically coincides with the emplacement of the volumetrically
626 major CAMP basalt extrusives in North America, Africa and Europe (Panfili et al.,
627 2019), and the development of anoxic–euxinic conditions in several marginal marine
628 basins at that time (Richoz et al., 2012; Blackburn et al., 2013; Jaraula et al., 2013;
629 Kasprak et al., 2015; Jost et al., 2017; Kent et al., 2017). This shift to more positive
630 carbon-isotope values is observed globally in carbonate and marine and terrestrial
631 organic matter, including primary skeletal calcite and terrestrial higher-plant
632 molecular *n*-alkanes (Figures 2, 3 and 6; Hesselbo et al., 2002; Yin et al., 2006;
633 Ward et al., 2007; Williford et al., 2007; Guex et al., 2008; van de Schootbrugge et
634 al., 2008; Korte et al., 2009; Ruhl et al., 2009; Whiteside et al., 2010; Bartolini et al.,
635 2012; Lindström et al., 2012; Felber et al., 2015; Yager et al., 2017; Ge et al., 2018;
636 Hesselbo et al., 2020). Enhanced marine productivity and preservation in
637 geographically more widespread anoxic–euxinic settings at this time, with the
638 associated elevated sequestration of isotopically light carbon into marine marls and
639 shales, may have acted as a powerful negative feedback in the global climate system
640 and carbon cycle. This phenomenon, which would have potentially driven the carbon
641 in the ocean–atmosphere system to more ^{13}C-enriched values, manifestly
642 complicates geochemical and mass-balance constraints on the magnitude and
643 source of isotopically light carbon released at this time.
644 The 2–3‰ exogenic carbon-cycle perturbation at the time of the end-Triassic
645 mass extinction likely resulted from carbon released primarily from (1) CAMP-basalt

volcanogenic carbon degassing (with a possible C-isotopic composition of ~-4 to -8‰; Macpherson and Mattey, 1994), (2) thermogenic methane release by the intrusion of CAMP-related dykes and sills into subsurface organic-rich shales (with a C-isotopic composition of ~-35 to -45‰), and/or (3) biogenic methane release from destabilizing sea-floor methane hydrates (with a C-isotopic composition of ~-60‰) (Coleman et al., 1981; Berner and Faber, 1987; Whiticar, 1999).

Previous studies have suggested that the negative CIE at the time of the end-Triassic mass extinction was relatively short in duration, with a rapid 10^3–10^4 yr onset (Deenen et al., 2010; Schoene et al., 2010; Ruhl et al., 2010; Whiteside et al., 2010; Yager et al., 2017). Simple mass-balance calculations presented here suggest that a ~2.5‰ negative shift in global exogenic $\delta^{13}C$ can be achieved with the release of ~20000 Gt C from methane hydrates or a larger mass of carbon as thermogenic methane or from volcanogenic sources (Figure 6; Supplementary Figure 3). Re-shuffling of carbon between Triassic–Jurassic carbon reservoirs, such as through the oxidation of terrestrial biomass, may have further contributed to a negative shift in global ocean–atmosphere carbon-isotope values. The doubling to tripling of atmospheric pCO_2 (from ~1000 to ~2000 ppmv based on stomatal-density analyses, or from ~2000 to ~6000ppmv based on pedogenic carbonate $\delta^{13}C$ (McElwain et al., 1999; Schaller et al., 2011; Steinthorsdottir et al., 2011; Schaller et al., 2012; Schaller et al., 2015), combined with a significant and rapid reduction in seawater pH (Črne et al., 2011; Hönisch et al., 2012; Ikeda et al., 2015) may, however, suggest that a much larger quantity of greenhouse gases was released at this time. Therefore, either (1) large amounts of carbon whose isotopic signature was similar to that of the ocean–atmosphere system (such as volcanogenic CO and CO_2) were released, or (2) large amounts of isotopically depleted carbon (such as thermo- or biogenic methane (CH_4)) were released, but this was largely offset by contemporaneous burial of isotopically light organic matter, resulting in a net reduction in the amplitude of the observed negative shift in $\delta^{13}C$ of global exogenic carbon reservoirs. A simple mass-

674 balance calculation suggests that ~13 × 10^5 Gt of organic carbon, with a carbon-
675 isotope composition of ~-25‰, had to have been buried over about 200 kyr, to
676 explain the observed positive excursion in $\delta^{13}C$ (following the end-Triassic mass
677 extinction and associated negative CIE) around the Triassic–Jurassic transition.
678 Such a carbon-burial flux, approximately half of the current yearly anthropogenic
679 carbon release, may be an underestimate of the actual figure. Even higher rates of
680 organic-carbon burial may have taken place at the time, explaining the short duration
681 and relatively small (2–3‰) magnitude of the 'initial' negative CIE at the end-Triassic
682 mass extinction interval. Actual quantitative analytical constraints on global (organic)
683 carbon-burial rates across the Triassic–Jurassic transition do not currently exist.
684 Accurate and precise constraints on (changes in) atmospheric pCO_2, and ocean pH
685 levels are essential to constrain the Triassic–Jurassic carbon-cycle evolution and
686 evaluate the magnitude and rate of change in carbon fluxes between the exogenic
687 carbon reservoirs, in response to CAMP magmatism.
688
689 **[5] CONCLUSIONS**
690 A bio- and chemostratigraphically constrained and expanded Triassic–Jurassic
691 boundary succession from the Arroyo Alumbre section in the Rio Atuel Region of the
692 Neuquén Basin, Argentina, is here described. Carbon-isotope analyses of
693 sedimentary organic matter ($\delta^{13}C_{TOC}$) in this biostratigraphically well-constrained
694 section can be reliably used to correlate Triassic–Jurassic boundary successions
695 between the northern and southern hemisphere and the Panthalassic and Tethyan
696 realms. The level of the end-Triassic mass extinction, located with the help of newly
697 discovered ammonoid faunas, is marked by a limited (2–3‰) magnitude negative
698 CIE, similar to that found in other eastern Panthalassic basins as well as $\delta^{13}C_{CARB}$
699 records in the Tethys realm, but significantly smaller than observed in
700 contemporaneous Tethyan $\delta^{13}C_{TOC}$ negative CIEs of 5–6‰.

Possibly arid climatic conditions, extending between 60º northern and southern latitudes across the western Pangaean landmass, may have resulted in a predominantly marine organic matter flux to the sedimentary realm in eastern Panthalassic basins, and mixing and changing marine and terrestrial sources of organic matter can explain the observed larger amplitude negative CIE in $\delta^{13}C_{TOC}$ records from the Tethyan realm.

Relative enrichment of sedimentary Hg (and Hg/TOC) in the marine Neuquén Basin initiated before the end-Triassic mass extinction and associated negative CIE, and before the emplacement of CAMP basalt flows began in North America and Africa. Sedimentary Hg enrichments do appear to correlate with the onset of CAMP-associated dyke and sill emplacement, suggesting thermal alteration of intruded sedimentary piles or intrusive magma degassing as a potential major source of elevated Hg fluxes to the atmosphere at this time.

The Neuquén Basin may have been marked by the development of reducing water-column conditions allowing a build-up of organic matter on the sea floor around the Triassic–Jurassic transition as a result of increased marine primary productivity and/or increased preservation. Combined with similar observations across the Panthlassic margin and the northwest Tethyan seaway, the data from Argentina suggest potentially significantly elevated organic-carbon burial rates in a global context. Simple mass-balance calculations show that enhanced carbon burial rates at this time, beginning at or directly succeeding the time of the end-Triassic mass extinction, and in line with the major emplacement phase of CAMP basalts, can explain the observed evolution of the global exogenic carbon cycle across the Triassic–Jurassic transition.

FIGURE CAPTIONS

Figure 1 Triassic–Jurassic continental configuration and the geographical extent of Central Atlantic Magmatic Province (CAMP) magmatism (shown by the

729 brown shading), modified after Korte et al. (2019) and references therein. The
730 magnitude of the $\delta^{13}C_{TOC}$ negative CIE, concomitant with the end-Triassic mass
731 extinction, is given in *blue* for the Pangaean realm, in *black* for the Tethyan realm,
732 and in *green* for the terrestrial realm, whereas the magnitude of this CIE in $\delta^{13}C_{CARB}$
733 is given in *purple* (*this study*; Palfy et al., 2001; Hesselbo et al., 2002; Galli et al.,
734 2005; Yin et al., 2006; Williford et al., 2007; van de Schootbrugge et al., 2008; Korte
735 et al., 2009; Ruhl et al., 2009; Deenen et al., 2010; Whiteside et al., 2010; Deenen et
736 al., 2011; Črne et al., 2011; Bartolini et al., 2012; Lindström et al., 2012; Dal Corso et
737 al., 2014; Al-Suwaidi et al., 2016; Ge et al., 2018; Yager et al., 2017; Hu et al., 2020).
738 Values for maximum sedimentary Hg (ppb) and Hg/TOC (ppb/%) values are given
739 with the coloured stars (this study; Thibodeau et al., 2016; Percival et al., 2017). The
740 geographical extension of arid climate belts and vegetation patterns across the
741 western and central Pangean landmass, at the time of the Triassic–Jurassic
742 transition, and the potentially expanded Hadley Cells under conditions of enhanced
743 greenhouse warming, are from Chandler et al., 1992; Rees et al., 2000; Huynh and
744 Poulsen, 2005; Sellwood and Valdes, 2006; Hu and Fu, 2007; Lu et al., 2007; Previdi
745 and Liepert, 2007; Kang and Lu, 2012; Sellwood and Valdes, 2008.
746
747 **Figure 2** Bio- and chemostratigraphical, and geochemical data across the
748 Triassic–Jurassic transition in the Arroyo Alumbre succession of the Neuquén Basin,
749 Argentina. Lithological columns presented here are from Riccardi et al. (2004), and
750 Damborenea and Manceñido (2012). Ammonoids collected from the studied section
751 constrain the age of the studied succession to span the Triassic–Jurassic transition
752 (Damborenea et al., 2017; and newly collected samples in Riccardi, 2019). Bivalve
753 diversity patterns show a significant decrease across the Triassic–Jurassic transition
754 (Damborenea et al., 2017 and references therein). An abrupt and stratigraphically
755 short-lived 2–3‰ negative excursion in $\delta^{13}C_{TOC}$ suggests that the stratigraphic
756 interval (in pink) represents the global end-Triassic mass extinction (*this study*).

757 Sedimentary zirconium (Zr) concentrations (*this study*) are relatively constant
758 throughout the studied succession, suggesting limited lithological change in the
759 studied shales and mudstones of the Arroyo Alumbre succession. Elevated
760 sedimentary Hg, Hg/TOC and Hg/Zr enrichments in strata stratigraphically preceding
761 this level suggest earlier CAMP-related magmatic activity (*this study*). Elevated total
762 organic carbon (TOC), and redox-sensitive trace and major element concentrations
763 (molybdenum (Mo and Mo/Zr) and sulphur (S and S/Zr)) suggest potential
764 environmental change and a possible shift toward more reducing conditions across
765 the end-Triassic mass extinction (*this study*).
766
767 **Figure 3** Bio- and chemostratigraphic and geochronological framework across
768 the Triassic–Jurassic transition in the Neuquén Basin (Argentina; *this study*), the
769 Bristol Channel Basin (UK; Hesselbo et al., 2002 and references therein), Levanto
770 (Peru; Yager et al., 2017), New York Canyon (USA; Bartolini et al., 2012 and
771 references therein; Thibodeau et al., 2016) and the Eiberg Basin (Austria; Ruhl et al.,
772 2009; Hillebrandt et al., 2013). Ash-bed ages from Levanto (Peru) and New York
773 Canyon (USA) are from [A, B, C, D] Wotzlaw et al. (2014), [E, F, G] Schaltegger et
774 al. (2008), Schoene et al. (2010), Wotzlaw et al. (2014), [H, I] Guex et al., 2012, [J]
775 Schoene et al. (2010).
776
777 **Figure 4** $\delta^{13}C_{TOC}$, $\delta^{13}C_{CARB}$ and $\delta^{13}C_{n\text{-alkane}}$ data across levels recording the end-
778 Triassic mass extinction and associated negative carbon-isotope excursion (CIE),
779 from marine successions in the Tethyan and Panthalassic realms and from terrestrial
780 successions in North America and northern Africa (*this study*; Hesselbo et al., 2002;
781 Galli et al., 2005; Williford et al., 2007; Ruhl et al., 2009; Deenen et al., 2010; Črne et
782 al., 2011; Deenen et al., 2011; Ruhl et al., 2011; Bartolini et al., 2012; Lindström et
783 al., 2012; van de Schootbrugge et al., 2013; Dal Corso et al., 2014; Felber et al.,
784 2015; Thibodeau et al., 2016; Suarez et al., 2017; Yager et al., 2017).

785

786 **Figure 5** [A] The magnitude of the negative carbon-isotope excursion in $\delta^{13}C$ of
787 total sedimentary organic carbon ($\delta^{13}C_{TOC}$), bulk-rock carbonate ($\delta^{13}C_{Carb}$) and leaf-
788 wax *n*-alkane biomarkers ($\delta^{13}C_{leaf\text{-}wax\ n\text{-}alkanes}$), with references referring to: (1)
789 Kennecott Point, Queen Charlotte Islands, Canada (Ward et al., 2001); (2) New York
790 Canyon, Nevada, USA (Ward et al., 2007); (3) Arroyo Alumbre, Argentina (This
791 study); (4) Pucara Basin, Peru (Yager et al., 2017); (5) Japan (Fujisaki et al., 2018);
792 (6) Newark & Hartford basins, USA (Whiteside et al., 2010); (7) Argana Basin,
793 Morocco (Deenen et al. (2010), Dal Corso et al. (2014)); (8) Fundy Basin, Canada
794 (Deenen et al., 2011); (9) Montenegro (Črne et al., 2011); (10) Hungary (Palfy et al.,
795 2001); (11) Italy (Galli et al., 2005); (12) Southern Tibet, China (Yin et al. 2006); (13)
796 Danish Basin, Denmark (Lindström et al., 2012); (14) German Basin, Germany (van
797 de Schootbrugge et al., 2008); (15) Italy (Bachan et al., 2012); (16) St Audries Bay,
798 Bristol Channel Basin, Somerset, UK (Hesselbo et al., 2002); (17) Restentalgraben,
799 Eiberg Basin, Austria (Ruhl et al., 2009); (18) Kuhjoch, Eiberg Basin, Austria (Ruhl et
800 al., 2011); (19) United Arab Emirates (Ge et al., 2018). [B] Model explaining how
801 organic-carbon source mixing pre- and post- the end-Triassic mass extinction could
802 have affected the magnitude of the associated negative carbon-isotope excursion
803 (CIE).

804

805 **Figure 6** Stratigraphical framework showing the long-term evolution of the
806 exogenic carbon cycle based on $\delta^{13}C_{TOC}$ data from the marine Arroyo Alumbre
807 (Neuquén Basin, Argentina) and St Audries Bay (Bristol Channel Basin, UK)
808 sections, marine $\delta^{13}C_{SKELETAL\ CALCITE}$ from Lavernock Point, Watchet and St Audries
809 Bay (Bristol Channel Basin, UK), terrestrial $\delta^{13}C_{TOC}$ from the continental Newark and
810 Hartford Basins (USA) (this study; Hesselbo et al., 2002; Korte et al., 2009; Ruhl et
811 al., 2010; Whiteside et al., 2010). Stratigraphical correlation between these sections
812 is also based on this study, Deenen et al. (2010), Whiteside et al. (2010), and Hüsing

et al. (2014). Also shown are reconstructed pCO_2 data from the Newark and Hartford Basins (USA) (Schaller et al., 2011, 2012, 2015), and Hg (and Hg/TOC) data from the (Neuquén Basin, Argentina, this study and Percival et al. (2017)). The stratigraphic occurrence of lavas of the Central Atlantic Magmatic Province (CAMP) and the age of the end-Triassic mass extinction are based on Davies et al. (2017), Kent et al. (2017 and references therein), and references in Xu et al. (2017*b*). The stratigraphic occurrence of elevated organic-carbon contents suggestive of low-oxygen conditions in marine basins during Triassic–Jurassic boundary times is based on references given in Section [4.4]. The computed $\delta^{13}C$ evolution of exogenic carbon reservoirs across the Triassic–Jurassic transition is based on simple mass-balance calculations, following different models as explained in the Supplementary Information section, incorporating the combined timed volcanogenic carbon release (with $\delta^{13}C$ = -5‰), biogenic methane release from ocean-floor clathrates (with $\delta^{13}C$ = -60‰), and elevated organic-carbon burial (with $\delta^{13}C$ = -35‰).

ACKNOWLEDGEMENTS

This research was financially supported by Shell International Exploration and Production BV. S.E.D., M.O.M. and A.C.R. were financially supported by CONICET (National Research Council of Argentina).

REFERENCES

Al-Suwaidi, A.H., Steuber, T., Suarez, M.B., The Triassic–Jurassic boundary event from an equatorial carbonate platform (Ghalilah Formation, United Arab Emirates). Journal of the Geological Society 173, 949–953 (2016).

Bachan, A., Payne, J.L., Modelling the impact of pulsed CAMP volcanism on pCO_2 and $\delta^{13}C$ across the Triassic–Jurassic transition. Geol. Mag. 153, 252–270 (2015).

Bachan, A., van de Schootbrugge, B., Fiebig, J., McRoberts, C.A., Ciarapica, G.,

841 Payne, J.L., Carbon cycle dynamics following the end-Triassic mas extinction:
842 Constraints from paired $\delta^{13}C_{carb}$ and $\delta^{13}C_{org}$ records. Geochemistry,
843 Geophysics, Geosystems 1 (9), Q09008 (2012), DOI:10.1029/2012GC004150.
844 Bagnato, E., Barra, M., Cardellini, C., Chiodini, G., Parello, F., Sprovieri, M., First
845 combined flux chamber survey of mercury and CO2 emissions from soil diffuse
846 degassing at Solfatara of Pozzuoli crater, Campi Flegrei (Italy): Mapping and
847 quantification of gas release. Journal of Volcanology and Geothermal Research
848 289, 26–40 (2014).
849 Barrón E., Gómez, J.J., Goy, A., Pieren, A.P., The Triassic–Jurassic boundary in
850 Asturias (northern Spain): Palynological characterisation and facies. Review of
851 Palaeobotany and Palynology 138, 187–208 (2006).
852 Bartolini, A., Guex, J., Spangenberg, J.E., Schoene, B., Taylor, D.G., Schaltegger,
853 U., Atudorei, V., Disentangling the Hettangian carbon isotope record:
854 Implications for the aftermath of the end-Triassic mass extinction.
855 Geochemistry, geophysics, Geosystems 13 (1), Q01007 (2012),
856 DOI:10.1029/2011GC003807.
857 Bechis, F., Giambiagi, L., García, V., Lanés, S., Cristallini, E., Tunik, M., Kinematic
858 analysis of a transtensional fault system: The Atuel depocenter of the Neuquén
859 basin, southern Central Andes, Argentina. Journal of Structural Geology 32,
860 886–899 (2010).
861 Berner, U., Faber, E., Maturity related mixing model for methane, ethane and
862 propane, based on carbon isotopes. Advances in Organic Geochemistry 13,
863 67–72 (1987).
864 Bin, C., Xiaoru, W., Lee, F.S.C., Pyrolyis coupled with atomic absorption
865 spectrometry for the determination of mercury in Chinese medicinal materials.
866 Analytica Chimica Acta 447, 161–169 (2001).
867 Blackburn, T.J., Olsen, P.E., Bowring, S.A., McLean, N.M., Kent, D.V., Puffer, J.,
868 McHone, G., Rasbury, E.T., Et-Touhami, M., Zircon U-Pb Geochronology Links

the End-Triassic Extinction with the Central Atlantic Magmatic Province. Science 340, 941–945 (2013).

Blum, J.D., Sherman, L.S., Johnson, M.W., Mercury isotopes in earth and environmental sciences: Annual Review of Earth and Planetary Sciences 42, 249–269 (2014).

Bonis, N.R., Kürschner, W.M., Krystyn, L., A detailed palynological study of the Triassic–Jurassic transition in key sections of the Eiberg Basin (Northern Calcareous Alps, Austria). Review of Palaeobotany and Palynology 156, 376–400 (2009).

Bonis, N.R., Kürschner, W.M., Vegetation history, diversity patterns, and climate change across the Triassic/Jurassic boundary. Paleobiology 38, 240–264 (2012).

Bonis, N.R., Ruhl, M., Kürschner, W.M., Climate change driven black shale deposition during the end-Triassic in the western Tethys. Palaeogeography, Palaeoclimatology, Palaeoecology 290, 151–159 (2010).

Bonis, N.R., Van Konijnenburg-Van Cittert, J.H.A., Kuerschner, W.M., Changing CO_2 conditions during the end-Triassic inferred from stomatal frequency analysis on *Lepidopteris ottonis* (Goeppert) Schimper and *Ginkgoites taeniatus* (Braun) Harris. Palaeogeography, Palaeoclimatology, Palaeoecology 295, 146–161 (2010).

Bowman, K.L., Hammerschmidt, C.R., Lamborg, C.H., Swarr, G., Mercury in the North Atlantic Ocean: The U.S. GEOTRACES zonal and meridional sections. Deep-Sea Research II 116, 251–261 (2015).

Chandler, M.A., Rind, D., Ruedy, R., Pangaean climate during the Early Jurassic: GCM simulations and the sedimentary record of paleoclimate. Geological Society of America Bulletin 104, 543–559 (1992).

Cirilli, S., Marzoli, A., Tanner, L., Bertrand, H., Buratti, N., Jourdan, F., Bellieni, G., Kontak, D., Renne, P.R., Latest Triassic onset of the central Atlantic Magmatic

897 Province (CAMP) volcanism in the Fundy Basin (Nova Scotia): New
898 stratigraphic constraints. Earth and Planetary Science Letters 286, 514–525
899 (2009).
900 Cirilli, S., Panfili, G., Buratti, N., Frixa, A., Paleoenvironmental reconstruction by
901 means of palynofacies and lithofacies analyses: An example from the Upper
902 Triassic subsurface succession of the Hyblean Plateau Petroleum System (SE
903 Sicily, Italy). Review of Palaeobotany and Palynology 253, 70–87 (2018).
904 Clémence, M.-E., Bartolini, A., Gardin, S., Paris, G., Beaumont, V., Page, K.N., Early
905 Hettangian benthic-planktonic coupling at Doniford (SW England)
906 palaeoenvironmental implications for the aftermath of the end-Triassic crisis.
907 Palaeogeography, Palaeoclimatology, Palaeoecology 295, 102–115 (2010).
908 Cohen, A.S., Coe, A.L., The impact of the Central Atlantic Magmatic Province on
909 climate and on the Sr- and Os-isotope evolution of seawater.
910 Palaeogeography, Palaeoclimatology, Palaeoecology 244, 374–390 (2007).
911 Coleman, D.D., Risatti, J.B., Schoell, M., Fractionation of carbon and hydrogen
912 isotopes by methane-oxidizing bacteria. Geochimica et Cosmochimica Acta 45,
913 1033–1037 (1981).
914 Črne, A.E., Weissert, H., Gorican, S., Bernasconi, S.M., A biocalcification crisis at the
915 Triassic–Jurassic boundary recorded in the Budva Basin (Dinarides,
916 Montenegro). Geological Society of America Bulletin 123, 40–50 (2011).
917 Dahl, T.W., Ruhl, M., Hammarlund, E.U., Canfield, D.E., Rosing, M.T., Bjerrum, C.J.,
918 Tracing euxinia by molybdenum concentrations in sediments using handheld X-
919 ray fluorescence spectroscopy (HHXRF). Chemical Geology 360–361,
920 241_251 (2013).
921 Dal Corso, J., Marzoli, A., Tateo, F., Jenkyns, H.C., Bertrand, H., Youbi, N.,
922 Mahmoudi, A., Font, E., Buratti, N., Cirilli, S., The dawn of CAMP volcanism
923 and its bearing on the end-Triassic carbon cycle disruption. J. Geol. Soc.171,
924 153–164 (2014).

925 Damborenea, S.E., Manceñido, M.O., Late Triassic bivalves and brachiopods from
926 southern Mendoza, Argentina. Revue de Paléobiologie, Genève 11, 317–344
927 (2012).
928 Damborenea, S.E., Echevarría, J., Ros-Franch, S., Biotic recovery after the end-
929 Triassic extinction event: Evidence from marine bivalves of the Neuquén Basin,
930 Argentina. Palaeogeography, Palaeoclimatology, Palaeoecology 487, 93–104
931 (2017).
932 Davies, J.H.F.L., Marzoli, A., Bertrand, H., Youbi, N., Ernesto, M., Schaltegger, U.,
933 End-Triassic mass extinction started by intrusive CAMP activity. Nature
934 Communications 8, 15596 (2017), DOI: 10.1038/ncomms15596.
935 Deenen, M.H.L., Krijgsman, W., Ruhl, M., The quest for chron E23r at Partridge
936 Island, Bay of Fundy, Canada: CAMP emplacement postdates the end-Triassic
937 extinction event at the North American craton. Can. J. Earth Sci., 48, 1282–
938 1291 (2011).
939 Deenen, M.H.L., Ruhl, M., Bonis, N.R., Krijgsman, W., Kuerschner, W.M., Reitsma,
940 M., van Bergen, M.J., A new chronology for the end-Triassic mass extinction.
941 Earth and Planetary Science Letters 291, 113–125 (2010).
942 Felber, R., Weissert, H.J., Furrer, H., Bontognali, T.R.R., The Triassic–Jurassic
943 boundary in the shallow-water marine carbonates from the western Northern
944 Calcareous Alps (Austria). Swiss J. Geosci. 108, 213–224 (2015).
945 Frenguelli, J., Estratigrafia y edad del llamado “Retico” en la Argentina. Rev. Soc.
946 Arg. Est. Geogr. GAEA, 8, 159-309 (1948).
947 Fujisaki, W., Matsui, Y., Asanuma, H., Sawaki, Y., Suzuki, K., Maruyama, S., Global
948 perturbations of carbon cycle during the Triassic–Jurassic transition recorded in
949 the mid-Panthalassa. Earth and Planetary Science Letters 500, 105–116
950 (2018).
951 Galli, M.T., Jadoul, F., Bernasconi, S.M., Weissert, H., Anomalies in global carbon
952 cycling and extinction at the Triassic/Jurassic boundary: evidence from a

marine C-isotope record. Palaeogeography, Palaeoclimatology, Palaeoecology 216, 203–214 (2005).

Ge, Y., Shi, M., Steuber, T., Al-Suwaidi, A.H., Suarez, M.B., Environmental change during the Triassic–Jurassic boundary interval of an equatorial carbonate platform: sedimentology and chemostratigraphy of the Ghalilah Formation, United Arab Emirates. Palaeogeography, Palaeoclimatology, Palaeoecology 502, 86–103 (2018).

Gómez, J.J., Goy, A., Barrón, E., Events around the Triassic–Jurassic boundary in northern and eastern Spain: A review. Palaeogeography, Palaeoclimatology, Palaeoecology 244 (1–4), 89–110 (2007).

Guex, J., Bartolini, A., Taylor, D., Atudorei, V., Thelin, P., Bruchez, S., Tanner, L., Lucas, S., Comment on: "The organic carbon isotopic and paleontological record across the Triassic–Jurassic boundary at the candidate GSSP section at Ferguson Hill, Muller Canyon, Nevada, USA" by Ward et al 2007. Palaeogeography, Palaeoclimatology, Palaeoecology 273, 200–204 (2008).

Guex, J., Schoene, B., Bartolini, A., Spangenberg, J., Schaltegger, U., O'Dogherty, L., Taylor, D., Bucher, H., Atudorei, V., Geochronological constraints on post-extinction recovery of the ammonoids and carbon cycle perturbations during the Early Jurassic. Palaeogeography, Palaeoclimatology, Palaeoecology 346–347, 1–11 (2012).

Greene, S.E., Martindale, R.C., Ritterbush, K.A., Bottjer, D.J., Corsetti, F.A., Berelson, W.M., Recognising ocean acidification in deep time: An evaluation of the evidence for acidification across the Triassic–Jurassic boundary. Earth-Science Reviews 113, 72–93 (2012).

Groeber, P., Descubrimiento del Triásico marino en la República Argentina. Comunicaciones del Museo de Historia Natural de Buenos Aires 2, 87–94 (1924).

Groeber, P., Líneas fundamentales de la geología del Neuquén, sur de Mendoza y

regiones adyacentes. Direc. Gen. Minas, Geol. e Hidrol. Publ. 58, 1–109, Buenos Aires (1929).

Groeber P., Stipanicic, P.N., Mingramm, A.G., Jurasico. *In* "Geografia de la Republica Argentina". Edic. Soc. Arg. Est. Geogr. GAEA, II (1), 143-347 (1953).

Heimdal, T.H., Svensen, H.H., Ramezani, J., Lyer, K., Pereira, E., Rodrigues, R., Jones, M.T., Callegaro, S., Large-scale sill emplacement in Brazil as a trigger for the end-Triassic crisis. Nature Scientific Reports 8, 141 (2018).

Hermoso, M., Callonnec, L.L., Minoletti, F., Renard, M., Hesselbo, S.P., Expression of the Early Toarcian negative carbon-isotope excursion in separated carbonate microfractions (Jurassic, Paris Basin). Earth and Planetary Science Letters 277, 194–203 (2009).

Hermoso, M., Pellenard, P., Continental weathering and climatic changes inferred from clay mineralogy and paired carbon isotopes across the early to middle Toarcian in the Paris Basin. Palaeogeography, Palaeoclimatology, Palaeoecology 399, 385–399 (2014).

Hesselbo, S.P., Robinson, S.A., Surlyk, F., Piasecki, S., Terrestrial and marine extinction at the Triassic–Jurassic boundary synchronized with major carbon-cycle perturbation: a link to initiation of massive volcanism? Geology 30, 251–254 (2002).

Hesselbo, S.P., Robinson, S.A., Surlyk, F., Sea-level change and facies development across potential Triassic–Jurassic boundary horizons, SW Britain. J. Geol. Soc. 161, 365–379 (2004).

Hesselbo, S.P., Korte, C., Ullmann, C.V., Ebbesen, A.L., Carbon and oxygen isotope records from the southern Eurasian Seaway following the Triassic–Jurassic boundary: Parallel long-term enhanced carbon burial and seawater warming. Earth-Science Reviews 203, 103131 (2020).

Hillebrandt, A.von., Krystyn, L., Kürschner, W.M., Bonis, N.R.4, Ruhl, M., Richoz, S.,

1009 Schobben, M.A.N., Urlichs, M., Bown, P.R., Kment, K., McRoberts, C.A.,
1010 Simms, M., Tomasových, A., The Global Stratotype Sections and Point (GSSP)
1011 for the base of the Jurassic System at Kuhjoch (Karwendel Mountains,
1012 Northern Calcareous Alps, Tyrol, Austria). Episodes 36, 162–198 (2013).
1013 Hönisch, B., Ridgwell, A., Schmidt, D.N., Thomas, E., Gibbs, S.J., Sluijs, A., Zeebe,
1014 R., Kump, L., Martindale, R.C., Greene, S.E., Kiessling, W., Ries, J., Zachos,
1015 J.C., Royer, D.L., Barker, S., Marchitto Jr., T.M., Moyer, R., Pelejero, C., Ziveri,
1016 P., Foster, G.L., Williams, B., The geological record of ocean acidification.
1017 Science 335, 1058 (2012).
1018 Howell, J.A., Schwarz, E., Spalletti, L.A., Veiga, G.D., The Neuquén Basin: an
1019 overview. In: Veiga, G.D., Spalletti, L.A., Howell, J.A. & Schwarz, E. (eds). The
1020 Neuquén Basin, Argentina: A Case Study in Sequence Stratigraphy and Basin
1021 Dynamics. Geological Society, London, Special Publications, 252, 1-14 (2005).
1022 Hu, Y., Fu, Q., Observed poleward expansion of the Hadley circulation since 1979.
1023 Atmos. Chem.Phys. 7, 5229–5236 (2007).
1024 Hu, F., Fu, X., Lin, L., Song, C., Wang, Z., Tian, K., Marine Late Triassic–Jurassic
1025 carbon-isotope excursion and biological extinction records: New evidence from
1026 the Qiangtang Basin, eastern Tethys. Global and Planetary Change 185,
1027 103093 (2020).
1028 Huang, C., Hesselbo, S.P., Pacing of the Toarcian Oceanic Anoxic Event (Early
1029 Jurassic) from astronomical correlation of marine sections. Gondwana
1030 Research 25, 1348–1356 (2014).
1031 Hüsing, S.K., Beniest, A., van der Boon, A., Abels, H.A., Deenen, M.H.L., Ruhl, M.,
1032 Krijgsman, W., Astronomically-calibrated magnetostratigraphy of the Lower
1033 Jurassic marine successions at St.Audrie's Bay and East Quantoxhead
1034 (Hettangian–Sinemurian; Somerset, UK). Palaeogeography,
1035 Palaeoclimatology, Palaeoecology 403, 43–56 (2014).
1036 Huynh, T.T., Poulsen, C., Rising atmospheric CO2 as a possible trigger for the end-

1037 Triassic mass extinction. Palaeogeography, Palaeoclimatology, Palaeoecology
1038 217, 223–242 (2005).
1039 Ikeda, M., Hori, R.S., Okada, Y., Nakada, R., Volcanism and deep-ocean
1040 acidification across the end-Triassic extinction event. Palaeogeography,
1041 Palaeoclimatology, Palaeoecology 440, 725–733 (2015).
1042 Jaraula, C.M.B., Grice, K., Twitchett, R.J., Böttcher, M.E., LeMetayer, P., Dastidar,
1043 A.G., Opazo, L.F., Elevated pCO_2 leading to Late Triassic extinction, persistent
1044 photic zone euxinia, and rising sea levels. Geology 41, 955–958 (2013).
1045 Jenkyns, H.C., Clayton, C.J., Black shales and carbon isotopes in pelagic sediments
1046 from the Tethyan Lower Jurassic. Sedimentology 33, 87–106 (1986).
1047 Jenkyns, H.C., The Early Toarcian (Jurassic) anoxic event: stratigraphic,
1048 sedimentary, and geochemical evidence. American Journal of Science 288,
1049 101–151 (1988).
1050 Jenkyns, H.C., Jones, C.E., Gröcke, D.R., Hesselbo, S.P., Parkinson, D.N.,
1051 Chemostratigraphy of the Jurassic System: applications, limitations and
1052 implications for palaeoceanography. Journal of the Geological Society, London
1053 159, 351–378 (2002).
1054 Jenkyns, H.C., Geochemistry of oceanic anoxic events. Geochemistry, Geophysics,
1055 Geosystems 11, Q03004, doi:10.1029/2009GC002788 (2010).Jones, M.T.,
1056 Percival, L.M.E., Stokke, E.W., Frieling, J., Mather, T.A., Riber, L., Schubert,
1057 B.A., Schultz, B., Tegner, C., Planke, S., Svensen, H.H., Mercury anomalies
1058 across the Palaeocene–Eocene Thermal Maximum. Clim. Pat 15, 217–236
1059 (2019).
1060 Jost, A.B., Bachan, A., van de Schootbrugge, B., Lau, K.V., Weaver, K.L., Maher, K.,
1061 Payne, J.L., Uranium isotope evidence for an expansion of marine anoxia
1062 during the end-Triassic extinction. Geochemistry, Geophysics, Geosystems 18
1063 (2017), DOI: 10.1002/2017GC006941.
1064 Kang, S.M., Lu, J., Expansion of the Hadley Cell under Global Warming: Winter

versus Summer. American Meteorological Society 25, 8387–8393 (2012).

Kasprak, A.H., Sepúlveda, J., Price-Waldman, R., Williford, K.H., Schoepfer, S.D., Haggart, J.W., Ward, P.D., Summons, R.E., Whiteside, J.H., Episodic photic zone euxinia in the mortheastern Panthalassic Ocean during the end-Triassic extinction. Geology 43, 307–310 (2015).

Kent, D.V., Santi Malnis, P., Colombi, C.E., Alcober, O.A., Martinez, R.N., Age constraints on the dispersal of dinosaurs in the Late Triassic from magnetochronology of the Los Colorados Formation (Argentina). Proc. Natl. Acad. Sci. 111 (22), 7958–7963 (2014).

Kent, D.V., Olsen, P.E., Muttoni, G., Astrochronostratigraphic polarity time scale (APTS) for the Late Triassic and Early Jurassic from continental sediments and correlation with standard marine stages. Earth-Science Reviews 166, 153–180 (2017).

Korte, C., Hesselbo, S.P., Jenkyns, H.C., Rickaby, R.E.M., Spötl, C., Palaeoenvironmental significance of carbon- and oxygen-isotope stratigraphy of marine Triassic Jurassic boundary sections in SW Britiain. Journal of the Geological Society 166, 431–445 (2009).

Korte, C., Kozur, H., Bio- and chemostratigraphic assessment of carbon isotope records across the Triassic–Jurassic boundary at Csővár quarry (Hungary) and Kendlbachgraben (Austria) and implications for global correlations. Bulletin of the Geological Society of Denmark 101–115 (2011).

Korte, C., Ruhl, M., Pálfy, J., Ullmann, C.V., Hesselbo, S.P., Chemostratigraphy Across the Triassic–Jurassic Boundary. In: Chemostratigraphy Across Major Chronological Boundaries, Geophysical Monograph 240, First Edition. Edited by Alcides N. Sial, Claudio Gaucher, Muthuvairavasamy Ramkumar, and Valderez Pinto Ferreira. American Geophysical Union. Published by John Wiley & Sons, Inc (2019).

Kuroda, J., Hori, R., Suzuki, K., Gröcke, D.R., Ohkouchi, N., Marine osmium isotope

record across the Triassic–Jurassic boundary from a Pacific pelagic site. Geology 38, 1095–1098 (2010).

Lanés, S., Giambiagi, L., Bechis, F., Tunik, M., Late Triassic–Early Jurassic successions of the Atuel depocenter: sequence stratigraphy and tectonic controls. Revista de la Asociación Geológica Argentina 63, 534–548 (2008).

Lanés, S., Late Triassic to Early Jurassic sedimentation in northern Neuquén Basin, Argentina: Tectosedimentary Evolution of the First Transgression. Geologica Acta 3, 81–106 (2005).

Leanza, A.F., El llamado Triásico marino de Brasil, Paraguay, Uruguay y la Argentina. Revista de la Asociación Geológica Argentina, Buenos Aires, 3: 219-244 (1948).

Leanza, H.A., Estratigrafía del Paleozoico y Mesozoico anterior a los movimientos intermálmicos en la comarca del Cerro Chachil, provincia del Neuquén. Revista de la Asociación Geológica Argentina, Buenos Aires 45 (3-4), 272-299 (1992).

Lindström, S., van de Schootbrugge, B., Dybkjaer, K., Pedersen, G.K., Fiebig, J., Nielsen, L.H., Richoz, S., No causal link between terrestrial ecosystem change and methane release during the end-Triassic mass extinction. Geology 40, 531–534 (2012).

Lourens, L.J., Sluijs, A., Kroon, D., Zachos, J.C., Thomas, E., Röhl, U., Bowles, J., Raffi, I., Astronomical pacing of late Palaeocene to early Eocene global warming events. Nature 435, 1083–1087 (2005).

Lu, J., Vecchi, G.A., Reichler, T., Expansion of the Hadley cell under global warming. Geophysical Research Letters 34, L06805 (2007).

Macpherson, C.G., Mattey, D.P., Carbon isotope variations of CO2 in Lau Basin basalts and ferrobasalts. Earth and Planetary Science Letters 121, 263–276 (1994).

Manceñido, M.O., Leanza, H.A., Formación Chachil. *In:* Riccardi, A.C., Damborenea, S.E. (Eds.), Léxico Estratigráfico de Argentina. Jurásico. Asociación Geológica

1121 Argentina, Serie B 21 (9), 137–139 (1993).
1122 Manceñido, M.O., Paleobiogeography of Mesozoic brachiopod faunas from Andean–
1123 Patagonian areas in a global context. Geobios Mémoire special 24, 176–192
1124 (2002).
1125 Mander, L., Kürschner, W.M., McElwain, J.C., An explanation for conflicting records
1126 of Triassic–Jurassic plant diversity. PNAS 107 (35), 15351–15356 (2010).
1127 Mander, L., Twitchett, R.J., Benton, M.J., Palaeoecology of the Late Triassic
1128 extinction event in the SW UK. Journal of the Geological Society, London 165,
1129 319–332 (2008).
1130 Mander, L., Twitchett, R.J., Quality of the Triassic–Jurassic bivalve fossil record in
1131 Northwest Europe. Palaeontology 51, 1213–1223 (2008).
1132 Marzoli, A., Bertrand, H., Knight, K.B., Cirilli, S., Buratti, N., Verati, C., Nomade, S.,
1133 Renne, O.R., Youbi, N., Martini, R., Allenbach, K., Neuwerth, R., Rapaille, C.,
1134 Zaninetti, L., Bellieni, G., Synchronocity of the Central Atlantic magmatic
1135 province and the Triassic–Jurassic boundary climatic and biotic crisis. Geology
1136 32 (11), 973–976 (2004).
1137 Marzoli, A., Jourdan, F., Puffer, J.H., Cuppone, T., Tanner, L.H., Weems, R.E.,
1138 Bertrand, H., Cirilli, S., Bellieni, G., De Min, A., Timing and duration of the
1139 Central Atlantic magmatic province in the Newark and Culpeper basins,
1140 eastern U.S.A. Lithos 122, 175–188 (2011).
1141 McElwain, J.C., Beerling, D.J., Woodward, F.I., Fossil plants and global warming at
1142 the Triassic–Jurassic boundary. Science 285, 1386 (1999).
1143 McElwain, J.C., Popa, M.E., Hesselbo, S.P., Haworth, M., Surlyk, F.,
1144 Macroecological responses of terrestrial vegetation to climatic and atmospheric
1145 change across the Triassic/Jurassic boundary in East Greenland. Paleobiology
1146 33 (4), 547–573 (2007),
1147 O'Keefe, J.M.K., Henke, K.R., Hower, J.C., Engle, M.A., Stracher, G.B., Stucker,
1148 J.D., Drew. J.W., Staggs, W.D., Murray, T.M., Hammond, M.L., Adkins, K.D.,

1149 Mullins, B.J., Lemley, E.W., CO_2, CO, and Hg emissions from the Truman
1150 Shepherd and Ruth Mullins coal fires, eastern Kentucky, USA. Science of the
1151 Total Environment 408, 1628–1633 (2010).
1152 Pálfy, J., Demény, A., Haas, J., Hetényi, M., Orchard, M.J., Vetö, I., Carbon isotope
1153 anomaly and other geochemical changes at the Triassic–Jurassic boundary
1154 from a marine section in Hungary. Geology 29, 1047–1050 (2001).
1155 Panfili, G., Cirilli, S., Dal Corso, J., Bertrand, H., Medina, F., Youbi, N., Marzoli, A.,
1156 New biostratigraphic constraints show rapid emplacement of the Central
1157 Atlantic Magmatic Province (CAMP) during the end-Triassic mass extinction
1158 interval. Global and Planetary Change 172, 60–68 (2019).
1159 Percival, L.M.E., Witt, M.L.I., Mather, T.A., Hermoso, M., Jenkyns, H.C., Hesselbo,
1160 S.P., Al-Suwaidi, A.H., Storm, M.S., Xu, W., Ruhl, M., Globally enhanced
1161 mercury deposition during the end-Pliensbachian and Toarcian OAE: A link to
1162 the Karoo–Ferrar Large Igneous Province. Earth and Planetary Science Letters
1163 428, 267–280 (2015).
1164 Percival, L.M.E., Ruhl, M., Hesselbo, S.P., Jenkyns, H.C., Mather, T.A., Whiteside,
1165 J.H., Mercury evidence for pulsed volcanism during the end-Triassic mass
1166 extinction. Proc. Nat. A. Sci. 114, 7929–7934 (2017).
1167 Percival, L.M.E., Jenkyns, H.C., Mather, T.A., Dickson, A.J., Batenburg, S.J., Ruhl,
1168 M., Hesselbo, S.P., Barclay, R., Jarvis, I., Robinson, S.A., Woelders, L., Does
1169 large igneous province volcanism always perturb the mercury cycle?
1170 Comparing the records of oceanic anoxic event 2 and the end-Cretaceous to
1171 other Mesozoic events. American Journal of Science 318, 799–860 (2018).
1172 Pérez, E., Reyes, R., Damborenea, S.E., El género Groeberella Leanza, 1993 y
1173 Groeberellidae nov. (Bivalvia; Trigonioida) del Jurásico de Chile y Argentina.
1174 Revista Geológica de Chile 22, 143-157, Santiago de Chile (1995).
1175 Peti, L., Thibault, N., Abundance and size changes in the calcareous nannofossil
1176 *Schizosphaerella* – Relation to sea-level, the carbonate factory and

palaeoenvironmental change from the Sinemurian to earliest Toarcian of the Paris Basin. Palaeogeography, Palaeoclimatology, Palaeoecology 485, 271–282 (2017).

Pienkowski, G., Biedzwiedski, G., Branski, P., Climatic reversals related to the Central Atlantic magmatic province caused the end-Triassic biotic crisis – Evidence from continental strata in Poland, *in* Keller, G., and Kerr, A., eds., Volcanism, Impacts, and Mass Extinctions: Causes and Effects: Geological Society of America Special Paper 505 (2014).

Previdi, M., Liepert, B.G., Annular modes and Hadley cell expansion under global warming. Geophysical Research Letters 34, L22701 (2007), DOI: 10.1029/2007GL031243.

Pyle, D.M., Mather, T.A., The importance of volcanic emissions for the global atmospheric mercury cycle. Atmospheric Environment 37, 5115–5124 (2003).

Rees, P.M.C.A., Ziegler, A.M., Valdes, P.J., Jurassic phytogeography and climates: new data and model comparisons. In: Huber, B.T., MacLeod, K.G., Wing, S.L. (Eds), Warm Climates in Earth History. Cambridge University Press (2000).

Riccardi, A.C., Damborenea, S.E., Mancenido, M.O., Ballent, S.C., Hettangiano y Sinemuriano marinos en Argentina. 5 Congreso Geológico Chileno Actas 2, 359–373 (1988).

.Riccardi, A.C., Damborenea, S.E., Manceñido, M.O., Ballent, S.C., Hettangian and Sinemurian (Lower Jurassic) biostratigraphy of Argentina. Journal of South American Earth Sciences 4, 159–170 (1991).

Riccardi, A.C., Damborenea, S.E., Manceñido, M.O., Scasso, R., Lanés, S., Iglesia Llanos, M.P., Primer registro de Triásico marino fosilífero de la Argentina. Revista de la Asociación Geológica Argentina 52 (2), 228–234 (1997).

Riccardi, A.C., Iglesia Llanos, M.P., Primer hallazgo de ammonites en el Triasico de la Argentina. Rev. Asoc. Geol. Argent. 54, 298–300 (1999).

1204 Riccardi, A.C., Damborenea, S.E., Manceñido, M.O., Iglesia Llanos, M.P., The
1205 Triassic/Jurassic boundary in the Andes of Argentina. Rivista Italiana di
1206 Paleontologia e Stratigrafia 110, 69–76 (2004).
1207 Riccardi, A.C., The marine Jurassic of Argentina: a biostratigraphic framework.
1208 Episodes 31, 326–335, Peking (2008).
1209 Riccardi, A.C., Damborenea, S.E., Manceñido, M.O., Leanza, H.A.,
1210 Megainvertebrados del Jurásico y su importancia geobiológica. Relatorio del
1211 XVIII Congreso Geológico Argentino, Neuquén, 441–464 (2011).
1212 Riccardi, A.C., Cephalopods from the Triassic–Jurassic boundary interval in west
1213 central Argentina. N.Jb. Geol. Paläont. Abh. 291/2, 135–157 (2019)
1214 Richoz, S., van de Schootbrugge, B., Pross, J., Püttmann, W., Quan, T.M.,
1215 Lindström, S., Heunisch, C., Fiebig, J., Maquil, R., Schouten, S.,
1216 Hauzenberger, C.A., Wignall, P.B., Hydrogen sulphide poisoning of shallow
1217 seas following the end-Triassic extinction. Nature Geoscience 5, 662–667
1218 (2012).
1219 Ruhl, M., Bonis, N.R., Reichart, G.-J., Sinninghe Damsté, J.S., Kürschner, W.M.,
1220 Atmospheric carbon injection linked to End-Triassic mass extinction. Science
1221 333, 430–434 (2011).
1222 Ruhl, M., Hesselbo, S.P., Hinnov, L., Jenkyns, H.C., Xu, W., Riding, J.B., Storm, M.,
1223 Minisini, D., Ullmann, C.V., Leng, M.J., Astronomical constraints on the
1224 duration of the Early Jurassic Pliensbachian Stage and global climatic
1225 fluctuations. Earth and Planetary Science Letters 455, 149–165 (2016).
1226 Ruhl, M., Kürschner, W.M., Krystyn, L., Triassic–Jurassic organic carbon isotope
1227 stratigraphy of key sections in the western Tethys realm (Austria). Earth and
1228 Planetary Science Letters 281, 169–187 (2009).
1229 Ruhl, M., Veld, H., Kürschner, W.M., Sedimentary organic matter characterization of
1230 the Triassic–Jurassic boundary GSSP at Kuhjoch (Austria). Earth and
1231 Planetary Science Letters 292, 17–26 (2010*a*).

1232 Ruhl, M., Deenen, M.H.L., Abels, H.A., Bonis, N.R., Krijgsman, W., Kürschner, W.M.,
1233 Astronomical constraints on the duration of the early Jurassic Hettangian stage
1234 and recovery rates following the end-Triassic mass extinction (St Audrie's Bay/
1235 East Quantoxhead, UK). Earth and Planetary Science Letters 295, 262–276
1236 (2010*b*).
1237 Schaller, M.F., Wright, J.D., Kent, D.V., A 30 myr record of Late Triassic atmospheric
1238 pCO_2 variation reflects a fundamental control of the carbon cycle by changes in
1239 continental weathering. Geological Society of America Bulletin 127, 661–671
1240 (2015).
1241 Schaller, M.F., Wright, J.D., Kent, D.V., Atmospheric pCO_2 perturbations associated
1242 with the Central Atlantic Magmatic Province. Science 331, 1404–1409 (2011).
1243 Schaller, M.F., Wright, J.D., Kent, D.V., Olsen, P.E., Rapid emplacement of the
1244 Central Atlantic Magmatic Province as a net sink for CO_2. Earth and Planetary
1245 Science Letters 323–324, 27–39 (2012).
1246 Schaltegger, U., Guex, J., Bartolini, A., Schoene, B., Ovtcharova, M., Precise U–Pb
1247 age constraints for end-Triassic mass extinction, its correlation to volcanism
1248 and Hettangian post-extinction recovery. Earth and Planetary Science Letters
1249 267, 266–275 (2008).
1250 Schroeder, W.H., Munthe J., Atmospheric mercury - An overview: Atmospheric
1251 Environment 32 (5), 809–822 (1998).
1252 Shen, S.-Z., Crowley, J.L., Wang, Y., Bowring, S.A., Erwin, D.H., Sadler, P.M., Cao,
1253 C.-Q, Rothman, D.H., Henderson, C., Ramezani, J., Zhang, H., Shen, Y.,
1254 Wang, X.-D., Wang, W., Mu, L., Li, W.-Z., Tang, Y.-G., Liu, X.-L., Liu, L.-J.,
1255 Zeng, Y., Jiang, Y.-F., Jin, Y.-G., Calibrating the End-Permian Mass Extinction.
1256 Science 334, 1367–1372 (2011).
1257 Schobben, M., Gravendyck, J., Mangels, F., Struck, U., Bussert, R., Kürschner,
1258 W.M., Korn, D., Sander, P.M., Aberhan, M., A comparative study of total
1259 organic carbon-δ13C signatures in the TriassicJurassic transitional beds of the

1260 Central European Basin and western Tethys shelf seas. Newsletters on
1261 Stratigraphy 52 (4), 461–486 (2019).
1262 Schoene, B., Guex, J., Bartolini, A., Schaltegger, U., Blackburn, T.J., Correlating the
1263 end-Triassic mass extinction and flood basalt volcanism at the 100 ka level.
1264 Geology 38, 387–390 (2010).
1265 Sellwood, B.W., Valdes, P.J., Mesozoic climates: General circulation models and the
1266 rock record. Sedimentary Geology 190, 269–287 (2006).
1267 Sellwood, B.W., Valdes, P.J., Jurassic climates. Proceedings of the Geologists'
1268 Association 119, 5–17 (2008).Steinthorsdottir, M., Jeram, A.J., McElwain, J.C.,
1269 Extremely elevated CO_2 concentrations at the Triassic/Jurassic boundary.
1270 Palaeogeography, Palaeoclimatology, Palaeoecology 308, 418–432 (2011).
1271 Steinthorsdottir, M., Woodward, F.I., Surlyk, F., McElwain, J.C., Deep-time evidence
1272 of a link between elevated CO_2 concentrations and perturbations in the
1273 hydrological cycle via drop in plant transpiration. Geology 40, 815–818 (2012).
1274 Storm, M., Hesselbo, S.P., Jenkyns, H.C., Ruhl, M., Ullmann, C.V., Xu, W., Leng,
1275 M.J., Riding, J.B., Gorbanenko, O., Orbital pacing and secular evolution of the
1276 Early Jurassic carbon cycle. Proc. Nat. A. Sci. 117, 3974–3982 (2020).
1277 Suan, G., van de Schootbrugge, B., Adatte, T., Fiebig, J., Oschmann, W., Calibrating
1278 the magnitude of the Toarcian carbon cycle perturbation. Paleoceanography
1279 30, 495–509 (2015).
1280 Suarez, C.A., Knobbe, T.K., Crowley, J.L., Kirkland, J.I., Milner, A.R.C., A
1281 chronostratigraphic assessment of the Moenave Formation, USA using C-
1282 isotope chemostratigraphic and detrital zircon geochronology: Implications for
1283 the terrestrial end Triassic extinction. Earth and Planetary Science Letters 475,
1284 83–93 (2017).
1285 Them II, T.R., Jagoe, C.H., Caruthers, A.H., Gill, B.C., Grasby, S.E., Gröcke, D.R.,
1286 Yin, R., Owens, J.D., Terrestrial sources as the primay delivery mechanism of

1287 mercury to the oceans across the Toarcian Oceanic Anoxic Event (Early
1288 Jurassic). Earth and Planetary Science Letters 507, 62–72 (2019).
1289 Thibodeau, A.M., Ritterbush, K., Yager, J.A., West, A.J., Ibarra, Y., Bottjer, D.J.,
1290 Berelson, W.M., Bergquist, B.A., Corsetti, F.A., Mercury anomalies and the
1291 timing of biotic recovery following the end-Triassic mass extinction. Nature
1292 Communications 7, 11147 (2016), DOI: 10.1038/ncomms11147.
1293 Tsikos, H., Jenkyns, H.C., Walsworth-Bell, B., Petrizzo, M.R., Forster, A., Kolonic, S.,
1294 Erba, E., Premoli Silva, I., Baas, M., Wagner, T., Sinninghe Damsté, J.S.,
1295 Carbon-isotope stratigraphy recorded by the Cenomanian–Turonian Oceanic
1296 Anoxic Event: correlation and implications based on three key localities.
1297 Journal of the Geological Society, London 161, 711–719 (2004).
1298 Tunik, M.A., Lanés, S., Bechis, F., Giambiagi, L. Análisis petrográfico de las
1299 areniscas Jurásicas tempranas en el depocentro Atuel de la Cuenca
1300 neuquina. Revista de la Asociación Geológica Argentina 63(4), 714–727
1301 (2008).
1302 van de Schootbrugge, B., Bailey, T.R., Rosenthal, Y., Katz, M.E., Wright, J.D., Miller,
1303 K.G., Feist-Burkhardt, S., Falkowski, P.G., Early Jurassic climate change and
1304 the radiation of organic-walled phytoplankton in the Tethys Ocean.
1305 Paleobiology 31, 73–97 (2005).
1306 van de Schootbrugge, B., Payne, J.L., Tomasovych, A., Pross, J., Fiebig, J.,
1307 Benbrahim, M., Föllmi, K.B., Quan, T.M., Carbon cycle perturbation and
1308 stabilization in the wake of the Triassic–Jurassic boundary mass-extinction
1309 event. Geochemistry, Geophysics, Geosystems 9, Q04028 (2008), DOI:
1310 10.1029/2007GC001914.
1311 van de Schootbrugge, B., Quan, T.M., Lindström, S., Püttmann, W., Heunisch, C.,
1312 Pross, J., Fiebig, J., Petschick, R., Röhling, H.-G.,, Richoz, S., Rosenthal, Y.,
1313 Falkowski, P.G., Floral changes across the Triassic/Jurassic boundary linked to

1314 flood basalt volcanism. Nature Geoscience 2, 589–594 (2009).
1315 van de Schootbrugge, B., Bachan, A., Suan, G., Richoz, S., Payne, J.L., Microbes,
1316 mud and methane: Cause and consequence of recurrent Early Jurassic anoxia
1317 following the end-Triassic mass extinction. Palaeontology 56, 685–709 (2013).
1318 van de Schootbrugge, B., Richoz, S., Pross, J., Luppold, F.W., Hunze, S., Wonik, T.,
1319 Blau, J., Meister, C., van der Weijst, C.M.H., Suan, G., Fraguas, A., Fiebig, J.,
1320 Herrle, J.O., Guex, J., Little, C.T.S., Wignall, P.B., Püttmann, W., Oschmann,
1321 W., The Schandelah Drilling Project: A 25-million year record of Early Jurassic
1322 palaeo-environmental change from northern Germany. Newsletters on
1323 Stratigraphy 52 (3), 249-296 (2019).
1324 Vergani, G.D., Tankard, A.J., Belotti, H.J., Welsink, H.J., Tectonic evolution and
1325 paleogeography of the Neuquén Basin, Argentina. American Association of
1326 Petroleum Geologists, Memoir 62, 383–402, Tulsa (1995).
1327 Vicente, J.C., Dynamic paleogeography of the Jurassic Andean Basin: pattern of
1328 transgression and localisation of main straits through the magmatic arc. Rev.
1329 de la Asoc. Geol. Argentina 60 (1), 221–250 (2005).
1330 Vicente, J.C., Dynamic paleogeography of the Jurassic Andean Basin: pattern of
1331 regression and general considerations on main features. Rev. de la Asoc.
1332 Geol. Argentina 61 (3), 408–437 (2006).
1333 Ward, P.D., Haggart, J.W., Carter, E.S., Wilbur, D., Tipper, H.W., Evans, T., Sudden
1334 productivity collapse associated with the Triassic–Jurassic boundary mass
1335 extinction. Science 292, 1148–1151 (2001).
1336 Ward, P.D., Garrison, G.H., Williford, K.H., Kring, D.A., Goodwin, D., Beattie, M.J.,
1337 McRoberts, C.A., The organic carbon isotopic and paleontological record
1338 across the Triassic–Jurassic boundary at the candidate GSSP section at
1339 Ferguson Hill, Muller Canyon, Nevada, USA. Palaeogeography,
1340 Palaeoclimatology, Palaeoecology 244, 281–289 (2007).

1341 Whiteside, J.H., Olsen, P.E., Eglinton, T., Brookfield, M.E., Sambrotto, R.N.,
1342 Compound-specific carbon isotopes from Earth's largest flood basalt eruptions
1343 directly linked to the end-Triassic mass extinction. Proc. Nat. A. Sci. 107,
1344 6721–6725 (2010).
1345 Whiticar, M., Carbon and hydrogen isotope systematics of bacterial formation and
1346 oxidation of methane. Chemical Geology 161, 291–314 (1999).
1347 Williford, K.H., Ward, P.D., Garrison, G.H., Buick, R., An extended organic carbon-
1348 isotopic record across the Triassic–Jurassic boundary in the Queen Charlotte
1349 Islands, British Columbia, Canada. Palaeogeography, Palaeoclimatology,
1350 Palaeoecology 244, 290–296 (2007).
1351 Wotzlaw, J.-F., Guex, J., Bartolini, A., Gallet, Y., Krystyn, L., McRoberts, C.A.,
1352 Taylor, D., Schoene, B., Schaltegger, U., Towards accurate numerical
1353 calibration of the Late Triassic: High-precision U-Pb geochronology constraints
1354 on the duration of the Rhaetian. Geology 42, 571-574 (2014).
1355 Xu, W., Ruhl, M., Jenkyns, H.C., Hesselbo, S.P., Riding, J.B., Selby, D., Naafs,
1356 B.D.A., Weijers, J.W.H., Pancost, R.D., Tegelaar, E.W., Idiz, E.F., Carbon
1357 sequestration in an expanded lake system during the Toarcian oceanic anoxic
1358 event. Nature Geoscience 10, pages 129–134 (2017*a*).
1359 Xu, W., Ruhl, M., Hesselbo, S.P., Riding, J.B., Jenkyns, H.C., Orbital pacing of the
1360 Early Jurassic carbon cycle, black-shale formation and seabed methane
1361 seepage. Sedimentology 64, 127–149 (2017*b*).
1362 Xu, W., Ruhl, M., Jenkyns, H.C.m Leng, M.J., Huggett, J.M., Minisini, D., Ullmann,
1363 C.V., Riding, J.B., Weijers, J.W.H., Storm, M., Percival, L.M.E., Tosca, N.J.,
1364 Idiz, E.F., Tegelaar, E.W., Hesselbo, S.P., Evolution of the Toarcian (Early
1365 Jurassic) carbon-cycle and global climatic controls on local sedimentary
1366 processes (Cardigan Bay Basin, UK). Earth and Planetary Science Letters 484,
1367 396–411 (2018).
1368 Yager, J.A., West, A.J., Corsetti, F.A., Berelson, W.M., Rollins, N.E., Rosas, S.,

1369 Bottjer, D.J., Duration of and decoupling between carbon isotope excursions
1370 during the end-Triassic mass extinction and Central Atlantic Magmatic Province
1371 emplacement. Earth and Planetary Science Letters 473, 227–236 (2017).
1372 Yin, J., Cai, H., Zhou, Z., Zhang, Y., Duan, X., Xie, Y., Study of marine
1373 Triassic/Jurassic boundary stratigraphy and the latest Triassic mass extinction
1374 in Tibet. Earth Science Frontiers 13, 244–254 (2006).

FIGURE 1

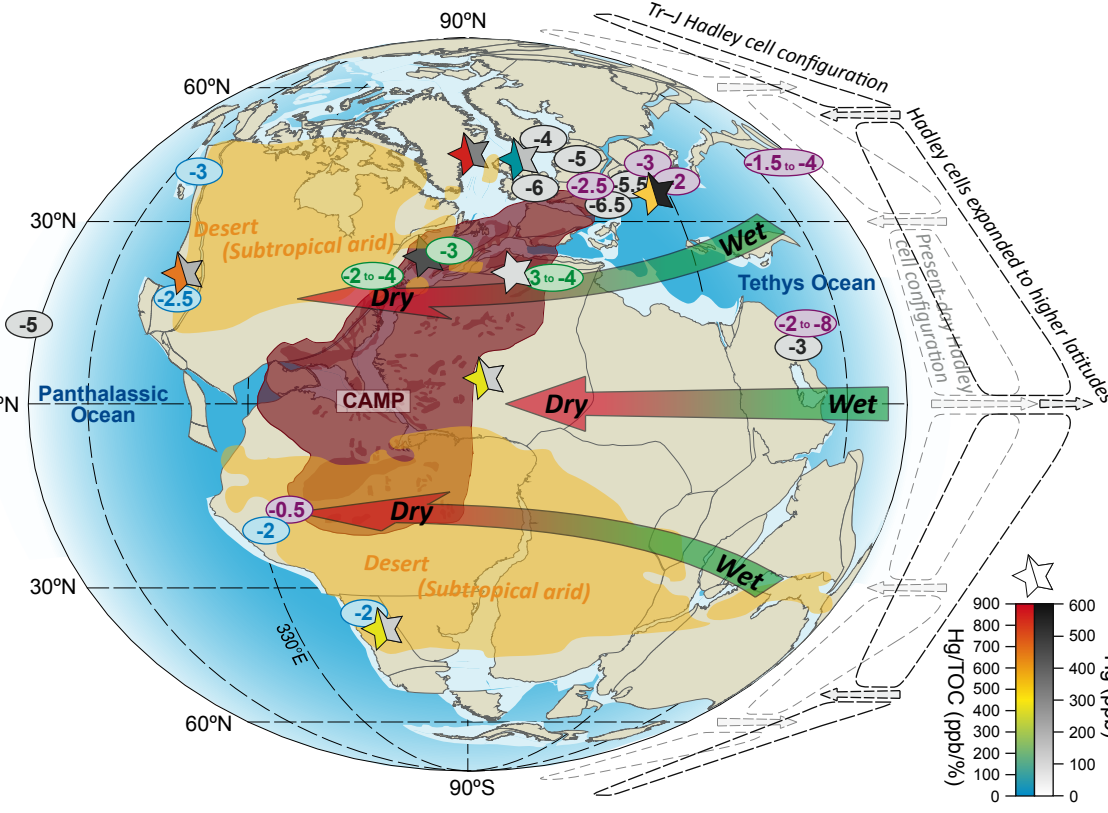
90°N
60°N
30°N
0°N
30°N
60°N
90°S
330°E
Tr–J Hadley cell configuration
Hadley cells expanded to higher latitudes
Present-day Hadley cell configuration
Desert (Subtropical arid)
Desert (Subtropical arid)
Wet
Dry
Dry
Wet
Dry
Wet
Tethys Ocean
Panthalassic Ocean
CAMP
-4
-5
-6
-3
-2.5
5.5
2
-6.5
-1.5 to -4
-3
-2.5
-5
-2 to -4
-3
3 to -4
-2 to -8
-3
-0.5
-2
-2
Hg/TOC (ppb/%)
900
800
700
600
500
400
300
200
100
0
Hg (ppb)
600
500
400
300
200
100
0

FIGURE 2

Arroyo Alumbre (Arroyo Malo), Neuquén Basin (Argentina)

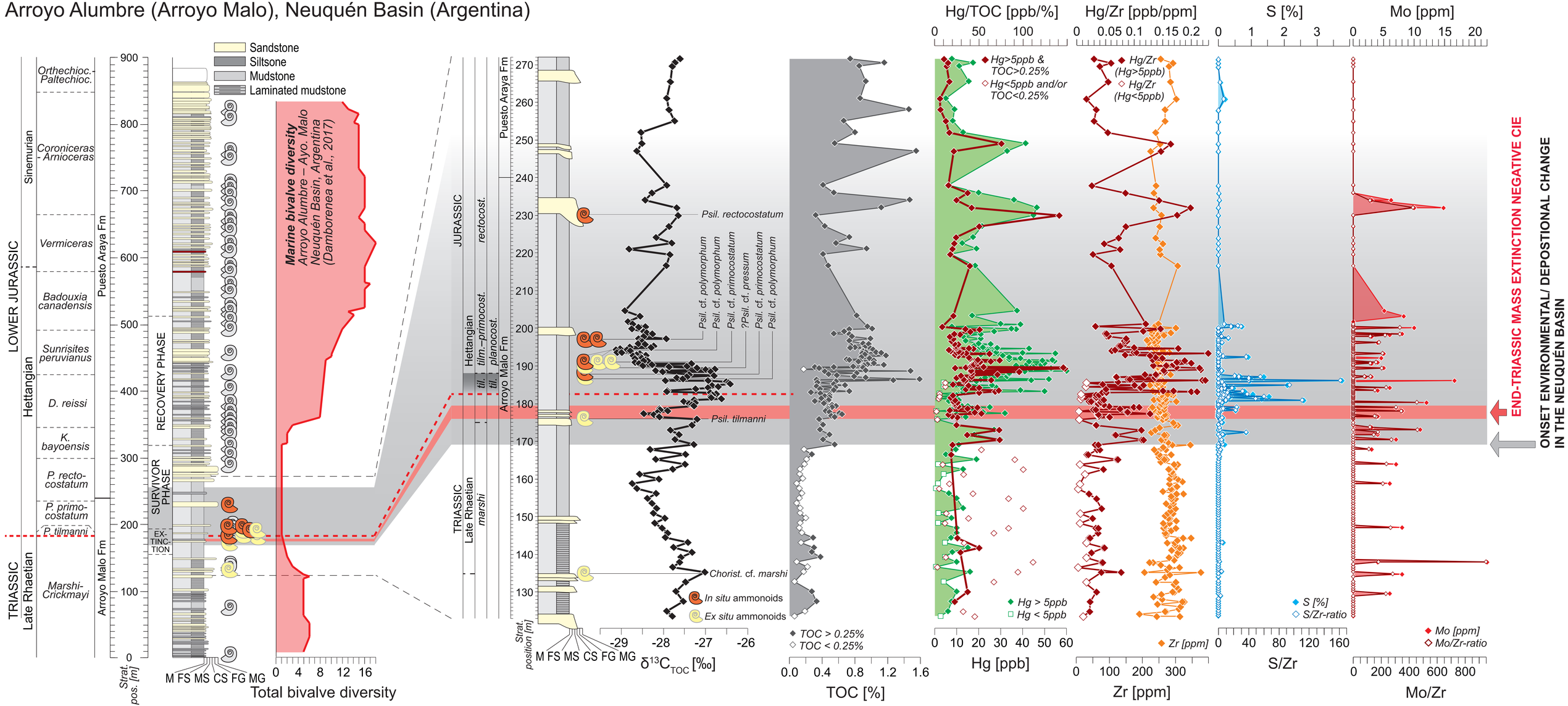

FIGURE 3

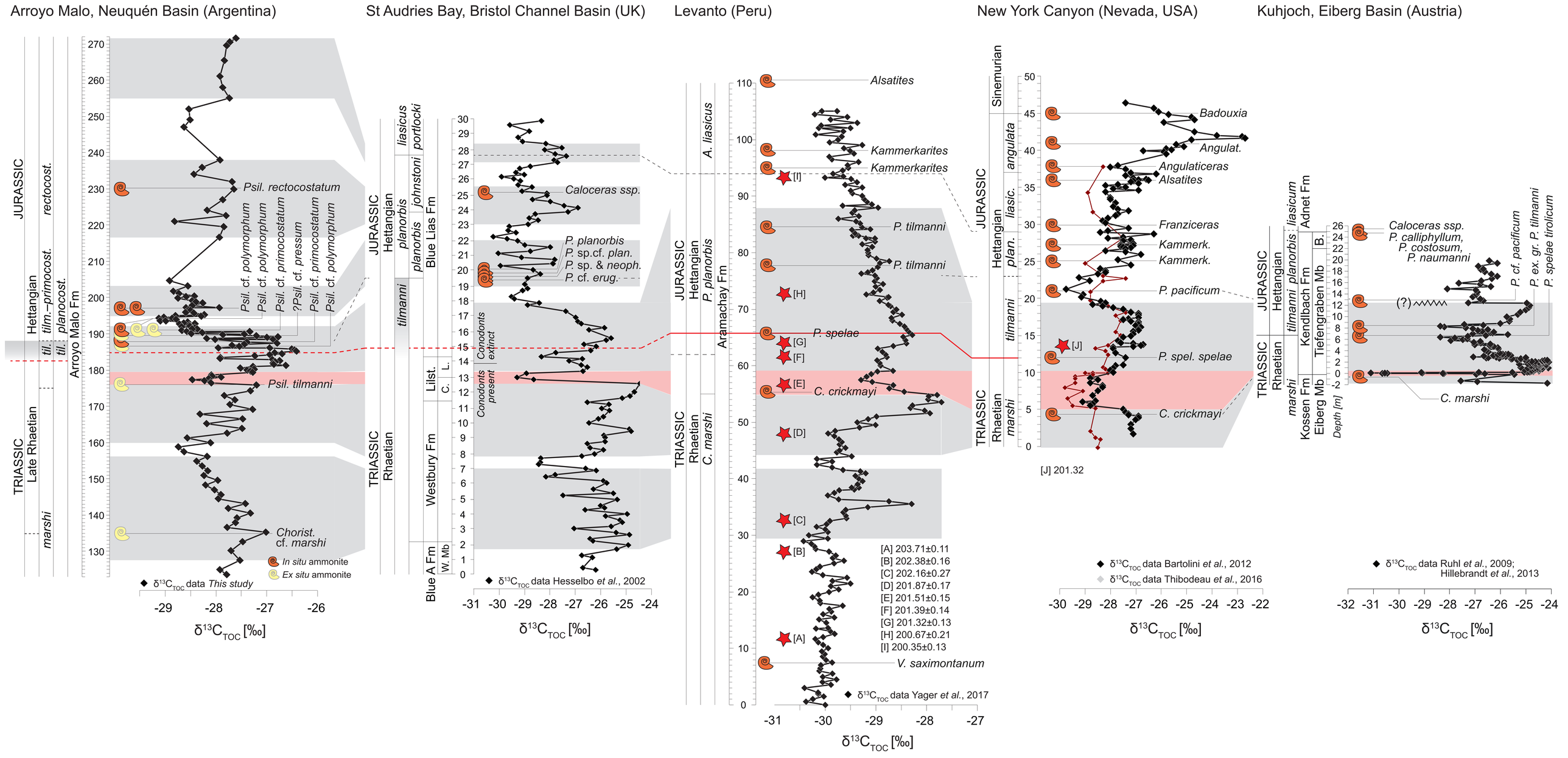
Arroyo Malo, Neuquén Basin (Argentina)
St Audries Bay, Bristol Channel Basin (UK)
Levanto (Peru)
New York Canyon (Nevada, USA)
Kuhjoch, Eiberg Basin (Austria)
JURASSIC
TRIASSIC
Hettangian
Late Rhaetian
Rhaetian
til.–primocost.
rectocost.
planocost.
marshi
Arroyo Malo Fm
Psil. rectocostatum
Psil. cf. polymorphum
Psil. cf. primocostatum
?Psil. cf. pressum
Psil. tilmanni
Chorist. cf. marshi
In situ ammonite
Ex situ ammonite
δ13CTOC data This study
liasicus
portlocki
johnstoni
planorbis
tilmanni
Blue Lias Fm
Westbury Fm
Lilst.
C.
L.
W. Mb
Blue A Fm
Caloceras ssp.
P. planorbis
P. sp.cf. plan.
P. sp. & neoph.
P. cf. erug.
Conodonts extinct
Conodonts present
δ13CTOC data Hesselbo et al., 2002
A. liasicus
P. planorbis
C. marshi
Aramachay Fm
Alsatites
Kammerkarites
[I]
P. tilmanni
[H]
P. spelae
[G]
[F]
[E]
C. crickmayi
[D]
[C]
[B]
[A]
V. saximontanum
[A] 203.71±0.11
[B] 202.38±0.16
[C] 202.16±0.27
[D] 201.87±0.17
[E] 201.51±0.15
[F] 201.39±0.14
[G] 201.32±0.13
[H] 200.67±0.21
[I] 200.35±0.13
δ13CTOC data Yager et al., 2017
Sinemurian
angulata
liasic.
plan.
Badouxia
Angulat.
Angulaticeras
Alsatites
Franziceras
Kammerk.
Kammerk.
P. pacificum
[J]
P. spel. spelae
C. crickmayi
[J] 201.32
δ13CTOC data Bartolini et al., 2012
δ13CTOC data Thibodeau et al., 2016
liasicum
planorbis
Adnet Fm
Kendlbach Fm
Kossen Fm
Eiberg Mb
B.
Tiefengraben Mb
Depth [m]
Caloceras ssp.
P. calliphyllum,
P. costosum,
P. naumanni
(?)
P. cf. pacificum
P. ex. gr. P. tilmanni
P. spelae tirolicum
C. marshi
δ13CTOC data Ruhl et al., 2009;
Hillebrandt et al., 2013
δ13CTOC [‰]

FIGURE 4

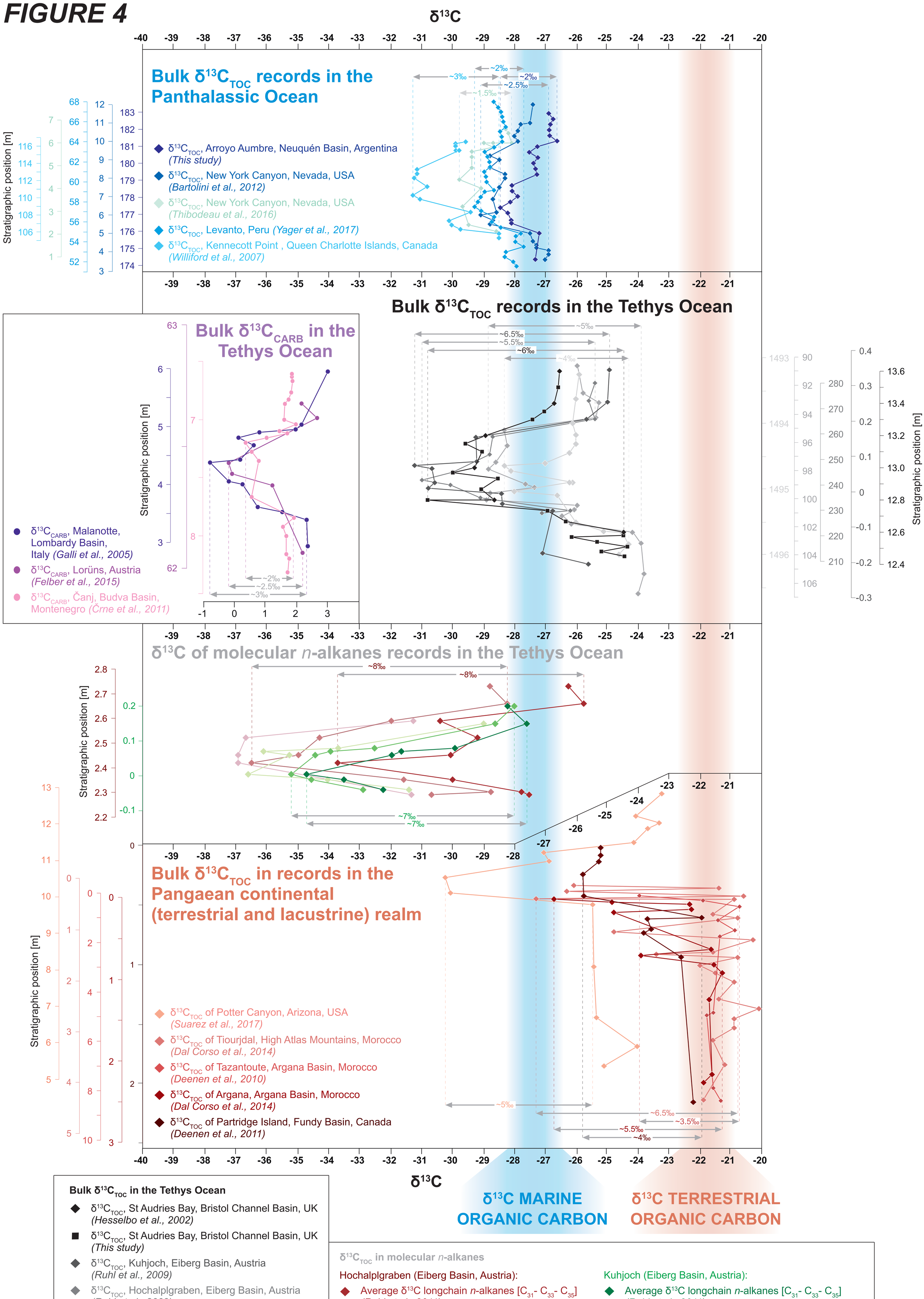

Bulk $\delta^{13}C_{TOC}$ in the Tethys Ocean

- $\delta^{13}C_{TOC}$, St Audries Bay, Bristol Channel Basin, UK *(Hesselbo et al., 2002)*
- $\delta^{13}C_{TOC}$, St Audries Bay, Bristol Channel Basin, UK *(This study)*
- $\delta^{13}C_{TOC}$, Kuhjoch, Eiberg Basin, Austria *(Ruhl et al., 2009)*
- $\delta^{13}C_{TOC}$, Hochalplgraben, Eiberg Basin, Austria *(Ruhl et al., 2009)*
- $\delta^{13}C_{TOC}$, Mariental, Germanic Basin, Germany *(van de Schootbrugge et al., 2013)*
- $\delta^{13}C_{TOC}$, Stenlille, Danish Basin, Denmark *(Lindström et al., 2012)*

$\delta^{13}C_{TOC}$ in molecular *n*-alkanes

Hochalplgraben (Eiberg Basin, Austria):

- Average $\delta^{13}C$ longchain *n*-alkanes [C_{31}- C_{33}- C_{35}] *(Ruhl et al., 2011)*
- Average $\delta^{13}C$ midchain *n*-alkanes [C_{23}- C_{25}- C_{27}- C_{29}] *(Ruhl et al., 2011)*
- Average $\delta^{13}C$ shortchain *n*-alkanes [C_{17}- C_{19}- C_{21}] *(Ruhl et al., 2011)*

Kuhjoch (Eiberg Basin, Austria):

- Average $\delta^{13}C$ longchain *n*-alkanes [C_{31}- C_{33}- C_{35}] *(Ruhl et al., 2011)*
- Average $\delta^{13}C$ midchain *n*-alkanes [C_{23}- C_{25}- C_{27}- C_{29}] *(Ruhl et al., 2011)*
- Average $\delta^{13}C$ shortchain *n*-alkanes [C_{17}- C_{19}- C_{21}] *(Ruhl et al., 2011)*

FIGURE 5

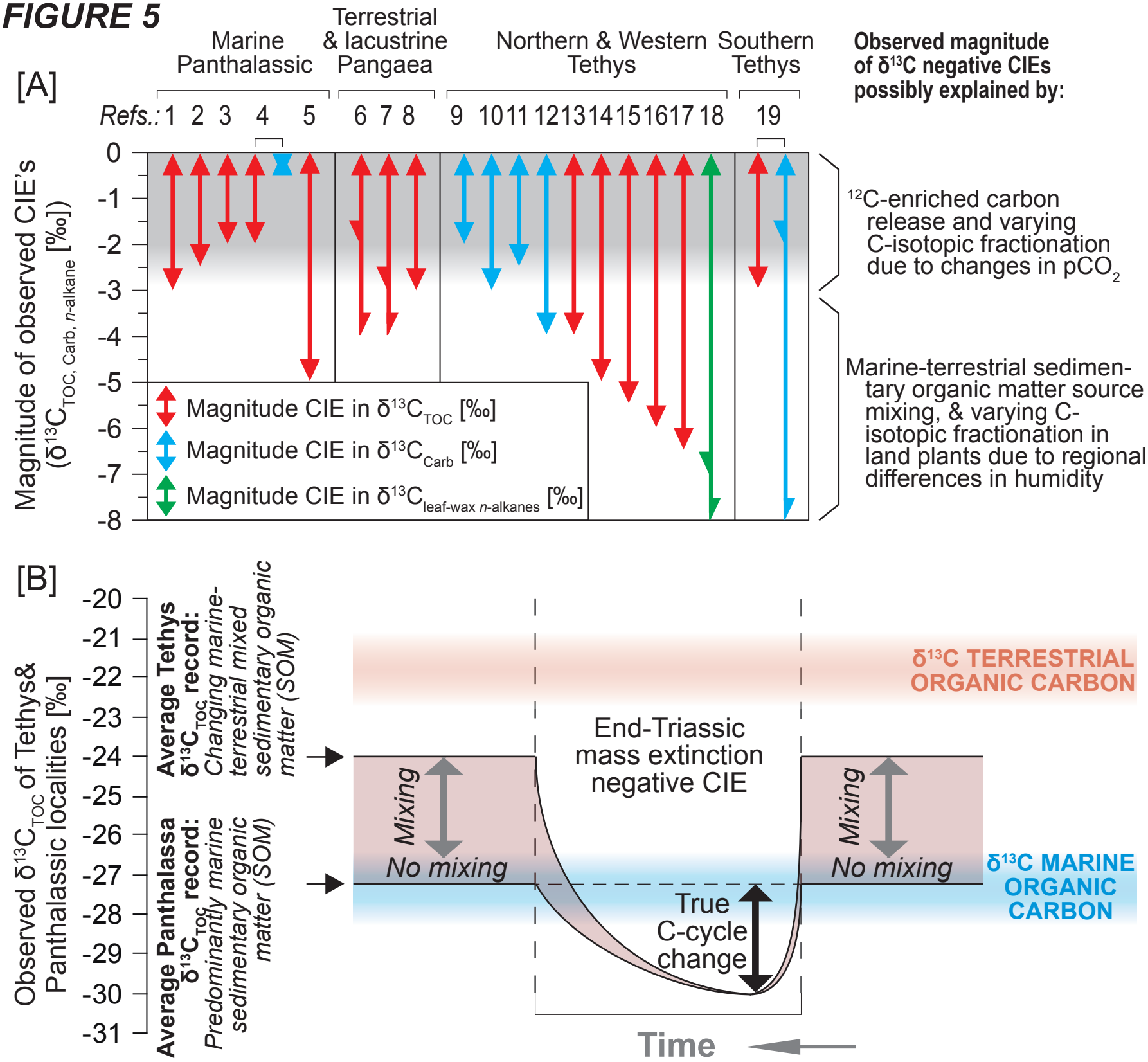
[A]
Marine Panthalassic
Terrestrial & lacustrine Pangaea
Northern & Western Tethys
Southern Tethys
Refs.: 1 2 3 4 5 6 7 8 9 10 11 12 13 14 15 16 17 18 19
Observed magnitude of δ13C negative CIEs possibly explained by:
Magnitude of observed CIE's (δ13CTOC, Carb, n-alkane [‰])
0
-1
-2
-3
-4
-5
-6
-7
-8
Magnitude CIE in δ13CTOC [‰]
Magnitude CIE in δ13CCarb [‰]
Magnitude CIE in δ13Cleaf-wax n-alkanes [‰]
12C-enriched carbon release and varying C-isotopic fractionation due to changes in pCO2
Marine-terrestrial sedimentary organic matter source mixing, & varying C-isotopic fractionation in land plants due to regional differences in humidity
[B]
Observed δ13CTOC of Tethys& Panthalassic localities [‰]
-20
-21
-22
-23
-24
-25
-26
-27
-28
-29
-30
-31
Average Tethys δ13CTOC record: Changing marine-terrestrial mixed sedimentary organic matter (SOM)
Average Panthalassa δ13CTOC record: Predominantly marine sedimentary organic matter (SOM)
δ13C TERRESTRIAL ORGANIC CARBON
End-Triassic mass extinction negative CIE
Mixing
No mixing
Mixing
No mixing
True C-cycle change
δ13C MARINE ORGANIC CARBON
Time

Figure 6

Relative time [kyr]

Computed Triassic–Jurassic carbon-cycle evolution in response to biogenic methane & CAMP volcanogenic carbon release, & enhanced carbon sequestration

Change in $\delta^{13}C$ [‰]

Biogenic methane release

Volcanogenic carbon release

Enhanced organic carbon sequestration

Neuquén Basin (Argentina)

Eiberg Basin (Austria)

Germanic Basin (Germany)

Kennecott Point (Canada)

Bristol Channel Basin (UK)

Enhanced organic carbon burial & Redox change in marginal marine basins

Kakoulima intrusion (Guinea)

Fouta Djalon sill (Guinea)

Tarabuco sill (Bolivia)

Messejana dyke (Spain)

Amazonas sill (Brazil)

Hodh sill (Mauritania)

Shelburne dyke (Canada)

Foum Zguid dyke (Morocco)

CAMP-basalt emplacement Fundy Basin (Canada)

CAMP-basalt emplace-ment Newark & Hartford Basin (USA)

CAMP-basalt emplace-ment Argana Basin/ High Atlas Mountains (Morocco)

CAMP magmatic activity

Onset of sedimentary Hg (and Hg/TOC) enrichments in the Neuquén Basin, Argentina

Hg/TOC (ppb/TOC)

Hg (ppb)

$\delta^{13}C_{TOC}$ [‰]

$\delta^{13}C_{Skeletal\ Calcite}$ [‰]

- Hg/TOC (ppb/TOC) from the marine Arroyo Alumbre (Neuquén Basin, Argentina)
- Hg (ppb) from the marine Arroyo Alumbre (Neuquén Basin, Argentina)
- $\delta^{13}C_{TOC}$ (‰) from the marine Arroyo Alumbre (Neuquén Basin, Argentina)
- $\delta^{13}C_{TOC}$ (‰) from the marine St Audries Bay (Bristol Channel Basin, UK)
- $\delta^{13}C_{TOC}$ (‰) from the terrestrial Newark and Hartford Basin (USA)
- pCO_2 (ppmv) from the terrestrial Newark and Hartford Basin (USA)

SA5n.1r SA5n.2r SA5n.3r SA5r

Magnetic polarity

Numerical time [Ma]

Westb. Fm. Blue Lias Formation

P. tilmanni *P. planorbis* *A. liasicus*

Rhaetian Hettangian

UPPER TRIASSIC LOWER JURASSIC

Atmospheric pCO_2 [ppmv]

E23r

Magnetic polarity

Numerical time [Myr]

Rhaetian Hettangian

TRIASSIC JURASSIC

End-Triassic mass extinction & negative CIE

SUPPLEMENTARY INFORMATION

ON THE ONSET OF CENTRAL ATLANTIC MAGMATIC PROVINCE (CAMP) VOLCANISM AND ENVIRONMENTAL AND CARBON-CYCLE CHANGE AT THE TRIASSIC–JURASSIC TRANSITION (NEUQUÉN BASIN, ARGENTINA)

Ruhl, M.[1,2], Hesselbo, S.P.[3], Al-Suwaidi, A.[4], Jenkyns, H.C.[2], Damborenea, S.E.[5], Manceñido, M.O.[5], Storm, M. [2,6], Mather, T.A.[2], Riccardi, A.C.[5]

[1] Department of Geology, Trinity College Dublin, The University of Dublin, College Green, Dublin 2, Dublin, Ireland

[2] Department of Earth Sciences, University of Oxford, South Park Road, OX1 3AN, Oxford, UK

[3] Camborne School of Mines and Environment and Sustainability Institute, University of Exeter, Penryn TR10 9FE, UK

[4] Petroleum Geoscience Department, Petroleum Institute and Research Centre, Khalifa University, PO Box 2533, Abu Dhabi, United Arab Emirates

[5] Departamento Paleontología Invertebrados, Museo de Ciencias Naturales La Plata, Paseo del Bosque s/n, 1900 La Plata, Argentina

[6] Department of Earth Sciences, Stellenbosch University, Stellenbosch 7600, South Africa

[1] MATERIALS & METHODS: $\delta^{13}C_{TOC}$, TOC, hh-XRF & Hg ANALYSES

[1.1] Materials

The Triassic–Jurassic sedimentary succession at Arroyo Alumbre was sampled during two field seasons (2014 and 2016). The Arroyo Alumbre (and associated nearby Arroyo Malo) sections were previously studied and described by Damborenea and Manceñido (2012, and references therein), who distinguished the Arroyo Malo Formation at the base (0–280m), stratigraphically overlain by the conglomeratic lenses of the El Freno Formation and the subsequent deposits of the El Cholo Formation.

The section is located high up in the Andes mountains, west of the main road from Malarguë to Mendoza (leaving the main road at El Sosneado), at 34°49'767''S – 69°53'224''W (Google-maps coordinates: -34.827675 (South), -69.888884 (West)) (Supplementary Materials Figures 1, 2-a, 2-b). The base of the relatively steep section is located at ~2395m above sea-level, on the western side of the Arroyo Alumbre valley (Supplementary Figures 2-c, d, e). The Arroyo Alumbre valley is a minor side-valley of the Arroyo Malo valley, which itself connects to the Rio Atuel to the south. The section can be accessed from El Sosneado along a ~38 km dirt-road along the Rio Atuel, followed by a ~1 hr hike (Supplementary Figure 2-a,b).

The Triassic–Jurassic sedimentary succession at Arroyo Alumbre represents a fully marine and stratigraphically expanded record (Figure 1). 42 samples (RA-1 to RA-42) were collected in 2014, from ~187m to ~272m in the section, and 160 additional samples (AA-1 to AA-160) were collected in 2016, from ~123m to ~205m in the section (Supplementary Figures 2-d,e).

[1.2] Fossil collections

All Triassic–Jurassic fossil material collected and described from the fossiliferous levels of the Arroyo Malo Formation at the Arroyo Alumbre/ Arroyo Malo localities, as

described in Damborenea et al. (2017, and references therein) and (Riccardi (2019, and references therein), are deposited in the collections of the Invertebrate Palaeontology Department of the La Plata Natural Sciences Museum (MLP).

[1.3] Bulk-rock organic $\delta^{13}C$ ($\delta^{13}C_{TOC}$) analysis

One gram of homogenized sample was treated with 40mL cold HCl (3 molar) to dissolve the carbonate. Samples (dissolved in 3 molar HCl) were then put on a hot plate for 2 hours at 80°C. Samples were subsequently rinsed 4 times with distilled water to reach neutral *p*H. Samples were then oven-dried (at 30°C) and again powdered. Around 1-15mg (depending on organic-carbon concentration) of homogenized de-carbonated sample residue was weighed into a 8×5-mm tin capsule $\delta^{13}C_{TOC}$ analyses. The $\delta^{13}C_{TOC}$ value of the samples was measured at the Stable Isotope Laboratory of the Open University (Milton Keynes, UK), with a Thermo Scientific Flash 2000 HT Elemental Analyzer (EA) coupled to a Thermo Scientific MAT253 isotope ratio mass spectrometer via a Conflo IV open split interface. The Thermo Scientific Flash 2000 HT EA has a MAS2000 carousel and between the carousel and the EA sits a Thermo No Blank Device (NBD), allowing for the single sample purging with helium. The EA is also equipped with a Thermal Conductivity Detector (TCD). Automated dilution of sample gas with the Conflo IV open split interface allows for high dynamic range of C+N content and controls the introduction of the “reference” gases. Isotope ratios are reported in standard delta notation relative to Vienna PDB.

Analytical precision was checked with the routine analysis of four internal and referenced laboratory standards (urea 020914MAG, IAEA-CH-6, NIST 8573, IRR041), showing measured average $\delta^{13}C_{TOC}$ values of -45.24‰, -10.39‰, -26.52‰, -23.58‰, respectively, and standard deviations of 0.85‰, 0.12‰, 0.28‰, 0.49‰.

[1.4] Rock-Eval: Total organic carbon (TOC)

Total organic carbon (TOC) analyses were performed using a Rock-Eval 6 Standard Analyser unit (Vinci Technologies), with pyrolysis and oxidation ovens, a flame ionization detector and infrared cell, at the Department of Earth Sciences, University of Oxford. The S1, S2, TMax, S3co/ S3co2 (New Oxygen Index), S4co/ S4co2 (Residual Organic Carbon), S5 (Mineral Carbon) are measured to calculate the Total Organic Carbon (TOC, in %), Hydrogen Index (HI, in mg HC/g TOC), and to characterize the kerogen types and other parameters. Laboratory procedures followed Behar et al. (2001). Around 50 mg of homogenized sample were weighed into crucibles and measured following a temperature profile of 300–650°C and 300–850°C for the pyrolysis and oxidation ovens, respectively. The IFP 160000 Reference Standard and the in-house SAB134 (Blue Lias organic-rich marl) standard were regularly measured (every 10 samples for the in-house standard). The standard deviation on TOC and HI of the in-house SAB134 and the reference IFP160000 standards is, respectively, 0.065% and 0.066% (TOC) and 22.65 mg HC/g TOC and 10.64 mg HC/g TOC (HI). The studied sediments are likely over-mature, with measured Tmax values of up to 577°C and with Production Index (PI) values being close to 1 in many samples and over 0.4 in all samples (Supplementary Materials).

[1.5] Mercury (Hg) analyses

Sedimentary mercury concentrations were analyzed on a RA-915 Portable Mercury Analyzer with PYRO-915 Pyrolyzer (Lumex), at the Department of Earth Sciences, University of Oxford, adapted from the methods described in Bin et al. (2001) and Percival et al. (2015). For each sample, about 50±2 mg of rock powder was weighed out and the precise mass recorded. For Hg-poor samples, about 100±2 mg of rock powder were analyzed. The material was heated in the Pyrolyzer to 700°C, volatilizing the mercury in the sample. The mercury gas was subsequently entered into the Analyzer, where its abundance was measured, allowing calculation of Hg concentration in the original mass of sample. The machine was calibrated

before use with six standards of peat (NIMT/UOE/FM/001 – Inorganic Elements in Peat) with Hg concentration of 169±7 ppb, of varying masses between 20 and 80 mg. During analysis, a further peat sample was analyzed after every ten rock samples to ensure continuity.

Previous Hg analyses from the Lower Jurassic sediments in the Arroyo Alumbre succession of the Neuquén Basin also showed relatively elevated Hg and Hg/TOC values (Percival et al., 2017). The expanded upper Triassic to lower Jurassic data-set presented here shows that some samples from the upper Triassic part of the succession are characterized by low Hg and/or TOC concentrations (Figure 2). The relative uncertainty in Hg and TOC analyses increases in samples with low respective concentration values. Hg/TOC values from samples with TOC < 0.25% and Hg < 5 ppb are therefore considered not trustworthy. Relatively elevated sedimentary Hg and Hg/TOC values, from samples with TOC > 0.25% and Hg > 5 ppb, already onset before the negative CIE associated with the end-Triassic mass extinction (Figure 2).

[1.6] Hand-Held X-Ray fluorescence (hh-XRF)

Hand-held X-Ray Fluorescence (hh-XRF) analysis was performed with the Olympus Innov-X Delta Premium XRF Analyzer, under climate-controlled laboratory conditions. The analyses were executed on both the flat surface of several cm^3-sized, hand specimens, as well as on the powdered material of each sample, throughout the studied section. The HH-XRF was run in 2 Beam Mining Mode (DS-6000) (each beam had a 40-sec measurement window; at 15 kV and 40 kV, respectively), and standard calibration to a manufacturer-delivered standard metal clip was performed at the onset of each run. Additionally, the NIST-2702 and NIST-2781 certified reference standards were regularly measured for quality control on the measurements, for calibration for long-term drift and measurement offset and to constrain measurement errors for the individual elements of interest. Frequent

measurements of the NIST-2702 standard show for calcium an average of 0.35% (NIST-2702 = 0.34%), with a standard deviation of 0.01%; for sulphur an average of 0.83% (NIST-2702 = 1.5%), with a standard deviation of 0.01%; and for molybdenum an average of 11ppm (NIST-2702 = 11.4ppm), with a standard deviation of 1.1ppm. Frequent measurements of the NIST-2781 standard show for calcium an average of 4.72% (NIST-2781 = 3.9%), with a standard deviation of 0.05%; for sulphur an average of 1.10%, with a standard deviation of 0.02%, and for molybdenum an average of 26.0ppm (NIST-2781 = 46.7ppm), with a standard deviation of 1.7ppm.

[2] SIMPLE MASS-BALANCE CACULATIONS ON TRIASSIC–JURASSIC CARBON-CYCLE EVOLUTION

The required release of isotopically light carbon, and the required changes in the fluxes between exogenic carbon reservoirs to explain the observed carbon cycle evolution across the Triassic–Jurassic transition, including the ~2.5‰ negative carbon isotope excursion (CIE) at the end-Triassic mass extinction and the subsequent positive CIE straddling the Triassic–Jurassic boundary, is tested using a simple mass balance calculation, under scenarios (1–4. Supplementary Figure 3):

- $d(\delta(Ex))/ dt = ((F_{additional}/ M_{ex}) \times (\delta_{additional} - \delta_{ex})) + ((F_{in}/ M_{ex}) \times (\delta_{in} – \delta_{ex})) – ((F_{out}/ M_{ex}) \times (\delta_{out} - \delta_{ex}))$

  - M_{ex} = Mass of exogenic carbon reservoirs (in Gt)
  - δ_{ex} = $\delta^{13}C$ composition of exogenic carbon reservoirs (in ‰)
  - F_{in} = Flux in (amount of carbon added to exogenic carbon reservoirs (in Gt/ 1000 yr)
  - δ_{in} = $\delta^{13}C$ composition of F_{in} (in ‰)
  - F_{out} = Flux out (amount of carbon extracted from exogenic carbon reservoirs (in Gt/ 1000 yr)

169 – δ_{out} = $\delta^{13}C$ composition of F_{out} (in ‰)

170 – $F_{additional}$ = Additional flux in (additional amount of carbon added to exogenic

171 carbon reservoirs (in Gt/ 1000 yr)

172 – $\delta_{additional}$ = $\delta^{13}C$ composition of $F_{additional}$ (in ‰)

173

174 (with M_{ex} and δ_{ex} at t=0 given as 60,000 Gt and -1 ‰, respectively, and other

175 parameters forced as given in Supplementary Figure 3).

176

177 **[3] SUPPLEMENTARY FIGURES**

178 **Supplementary Figure 1** Early Jurassic (Pliensbachian–Toarcian) basin

179 geometry and facies distribution of the Neuquén Basin, Argentina (modified after

180 Riccardi et al., 2011).

181

182 **Supplementary Figure 2-A** Location of the Arroyo Alumbre section in the Neuquén

183 Basin, Argentina (images from Google Earth).

184

185 **Supplementary Figure 2-B** Location of the Arroyo Alumbre section in the Neuquén

186 Basin, Argentina (images from Google Earth).

187

188 **Supplementary Figure 2-C** Outcrop photos of the Arroyo Alumbre section in the

189 Neuquén Basin, Argentina.

190

191 **Supplementary Figure 2-D** Outcrop photos of the Arroyo Alumbre section in the

192 Neuquén Basin, Argentina, with the stratigraphic position of the studied samples.

193

194 **Supplementary Figure 2-E** Outcrop photos of the Arroyo Alumbre section in the

195 Neuquén Basin, Argentina, with the stratigraphic position of the studied samples.

196

Supplementary Figure 3 Model output of the $\delta^{13}C$ evolution of exogenic carbon reservoirs across the Triassic–Jurassic transition, based on simple mass-balance calculations. The impact of timed volcanogenic-carbon release (with $\delta^{13}C$ = -5‰), biogenic methane release from dissociation of ocean-floor clathrates (with $\delta^{13}C$ = -60‰), and elevated organic-carbon burial (with $\delta^{13}C$ = -35‰), are evaluated separately. Colours represent the different scenarios and model outputs given in Figure 6 of the main text.

[4] REFERENCES

Behar, F., Beaumont, V., De B. Penteado, H.L., Rock-Eval 6 Technology: Performances and Developments. Oil & Gas Science and Technology – Rev. IFP 56 (2), 111–134 (2001).

Bin, C., Xiaoru, W., Lee, F.S.C., Pyrolysis coupled with atomic absorption spectrometry for the determination of mercury in Chinese medical materials. Anal. Chim. Acta 447, 161–169 (2001).

Damborenea, S.E., Echevarría, J., Ros-Franch, S., Biotic recovery after the end-Triassic extinction event: Evidence from marine bivalves of the Neuquén Basin, Argentina. Palaeogeography, Palaeoclimatology, Palaeoecology 487, 93–104 (2017).

Damborenea, S.E., Manceñido, M.O., Late Triassic bivalves and brachiopods from southern Mendoza, Argentina. Revue de Paléobiologie, Genève 11, 317–344 (2012).

Percival, L.M.E., Ruhl, M., Hesselbo, S.P., Jenkyns, H.C., Mather, T.A., Whiteside, J.H., Mercury evidence for pulsed volcanism during the end-Triassic mass extinction. PNAS 114, 7929–7934 (2017).

Percival, L.M.E., Witt, M.L.I., Mather, T.A., Hermoso, M., Jenkyns, H.C., Hesselbo, S.P., Al-Suwaidi, A.H., Storm, M.S., Xu, W., Ruhl, M., Globally enhanced mercury deposition during the end-Pliensbachian and Toarcian OAE: A link to

the Karoo–Ferrar Large Igneous Province. Earth and Planetary Science Letters 428, 267–280 (2015).

Riccardi, A.C., Damborenea, S.E., Manceñido, M.O., Leanza, H.A., Megainvertebrados del Jurásico y su importancia geobiológica. Relatorio del XVIII Congreso Geológico Argentino, Neuquén, 441–464 (2011).

Riccardi, A.C., Cephalopods from the Triassic–Jurassic boundary interval in west central Argentina. N.Jb. Geol. Paläont. Abh. 291/2, 135–157 (2019).

SUPPLEMENTARY FIGURE 1

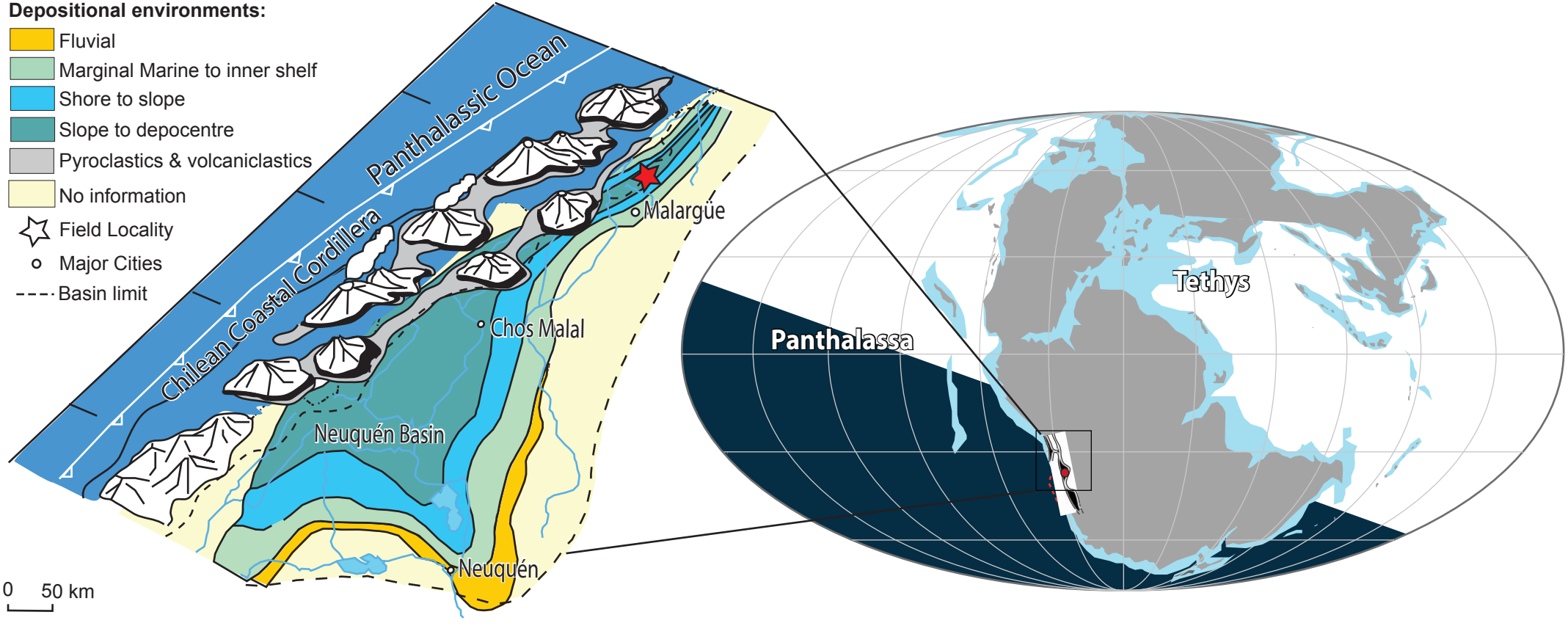

SUPPLEMENTARY FIGURE 2 A

Triassic–Jurassic boundary section at Arroyo Alumbre:
34°49’767’’S – 69°53’224’’W (Google-maps coordinates: -34.827675, -69.888884)

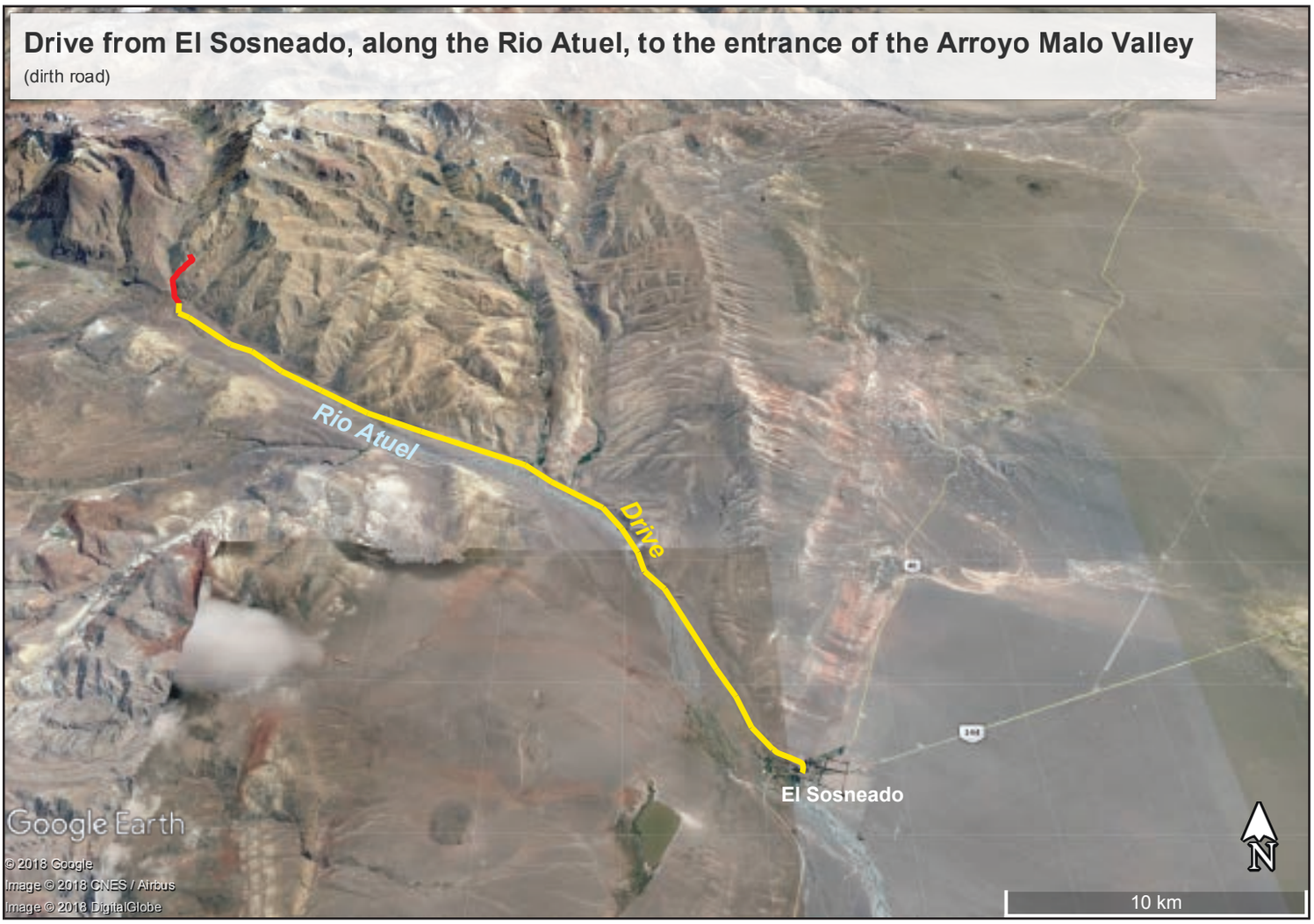

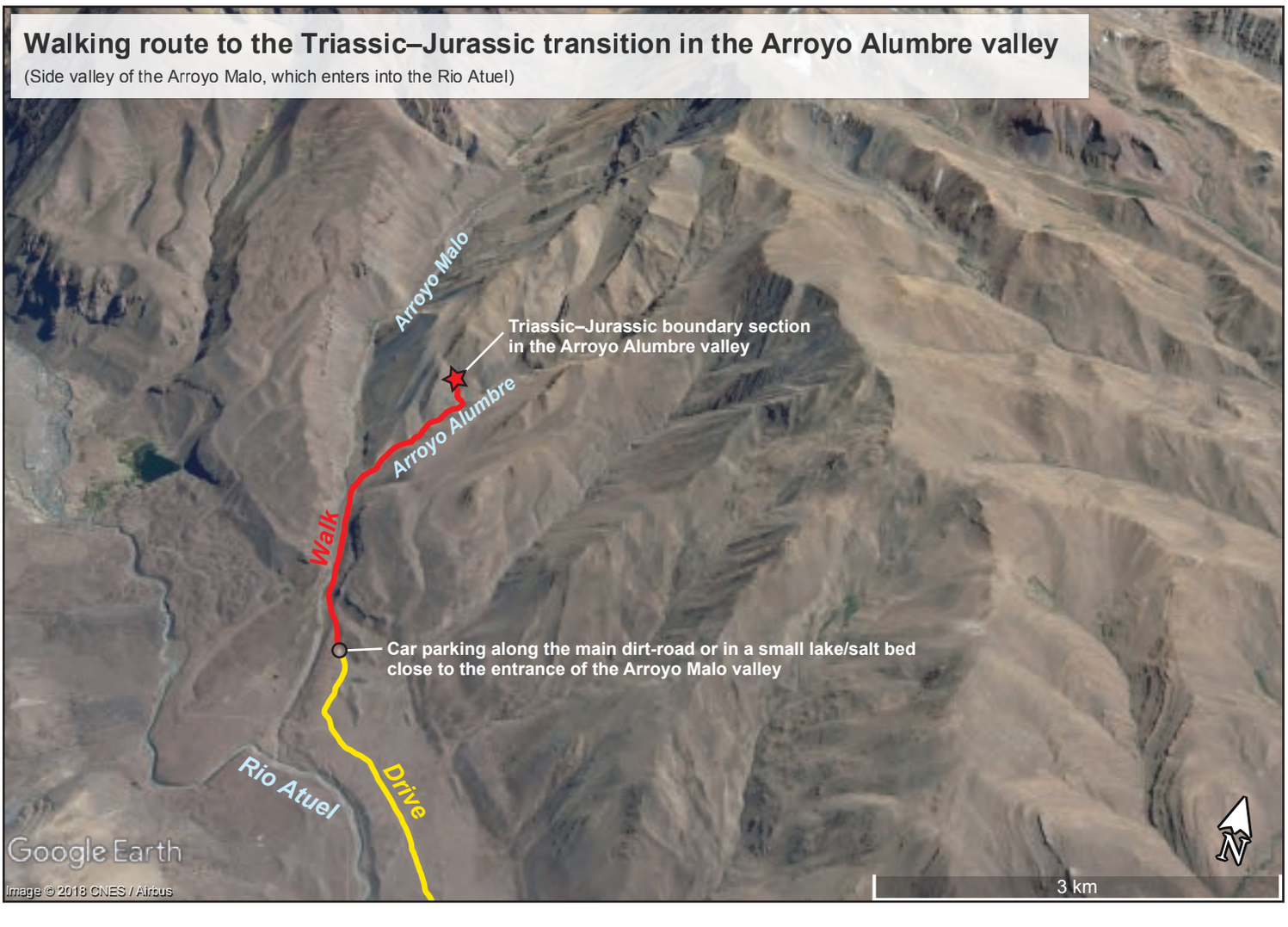

SUPPLEMENTARY FIGURE 2-B

Triassic–Jurassic boundary section at Arroyo Alumbre:
34°49’767’’S – 69°53’224’’W (Google-maps coordinates: -34.827675, -69.888884)

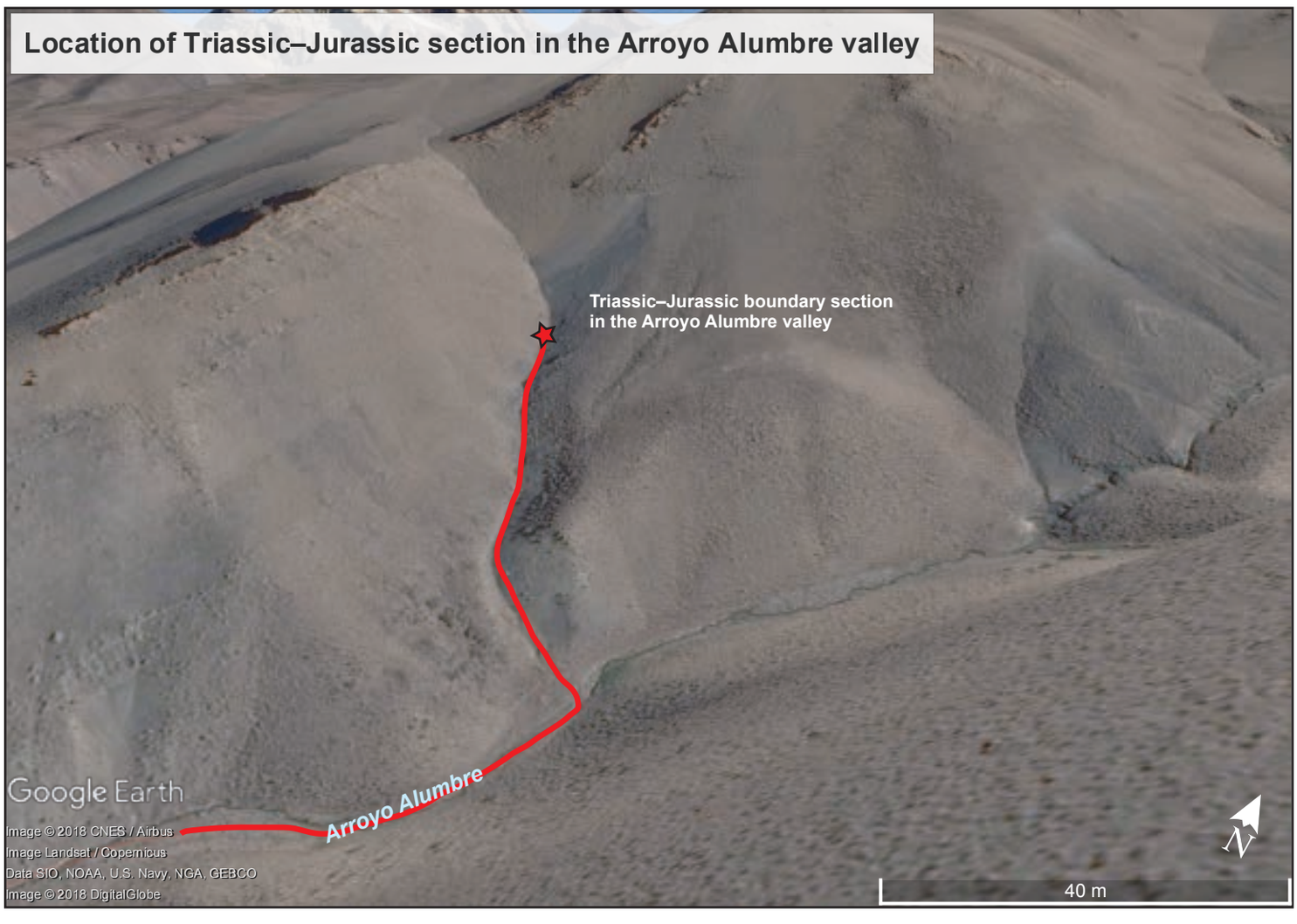

SUPPLEMENTARY FIGURE 2-C

Triassic–Jurassic boundary section at Arroyo Alumbre:
34°49’767”S – 69°53’224”W (Google-maps coordinates: -34.827675, -69.888884)

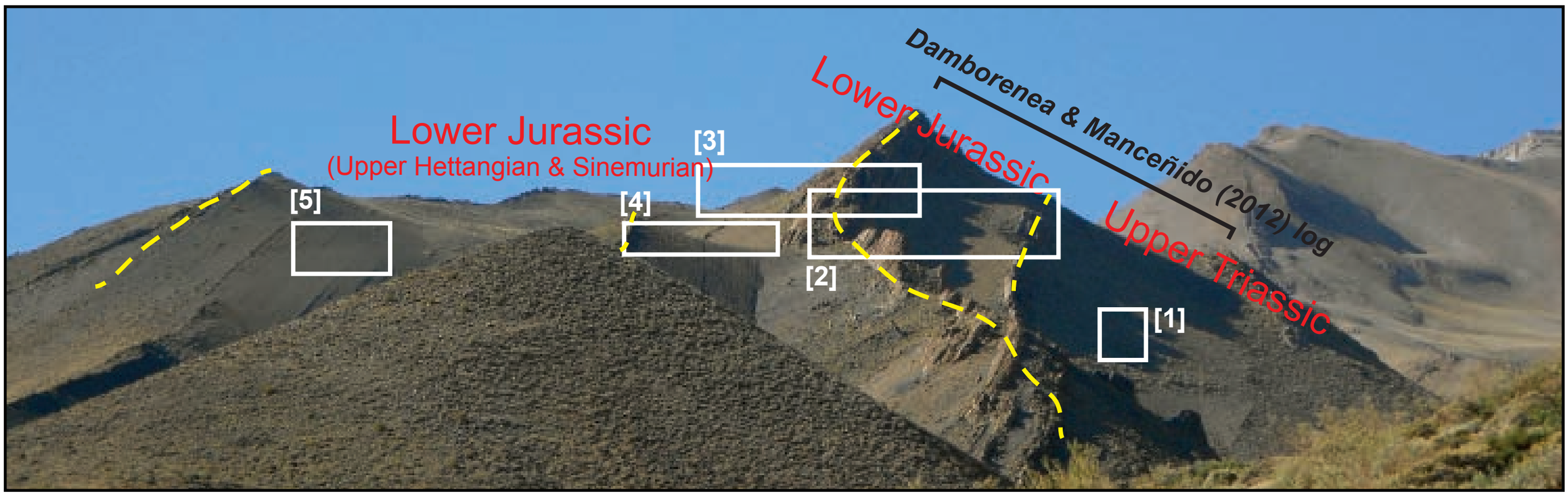

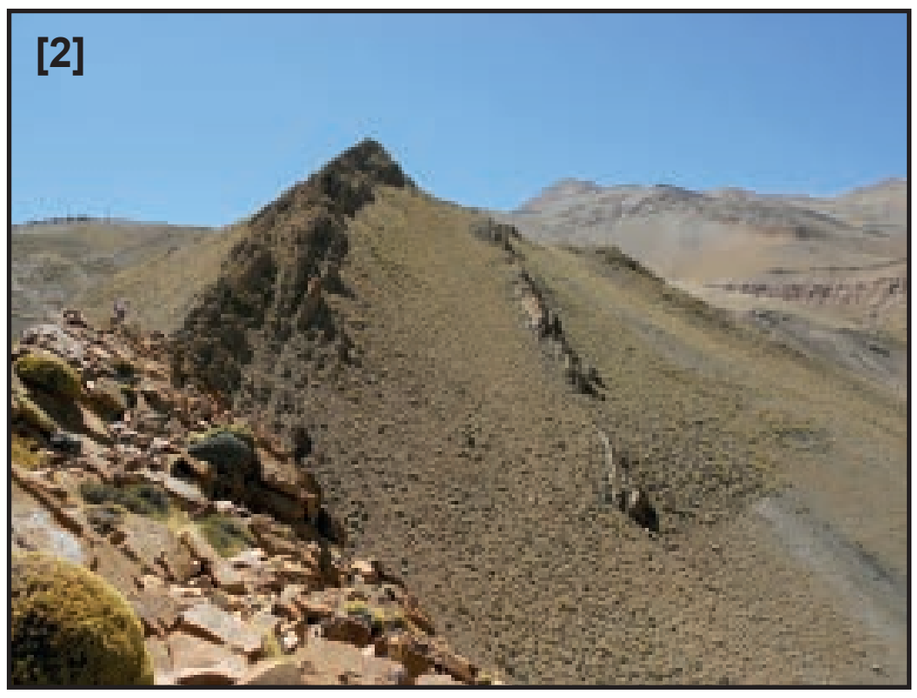

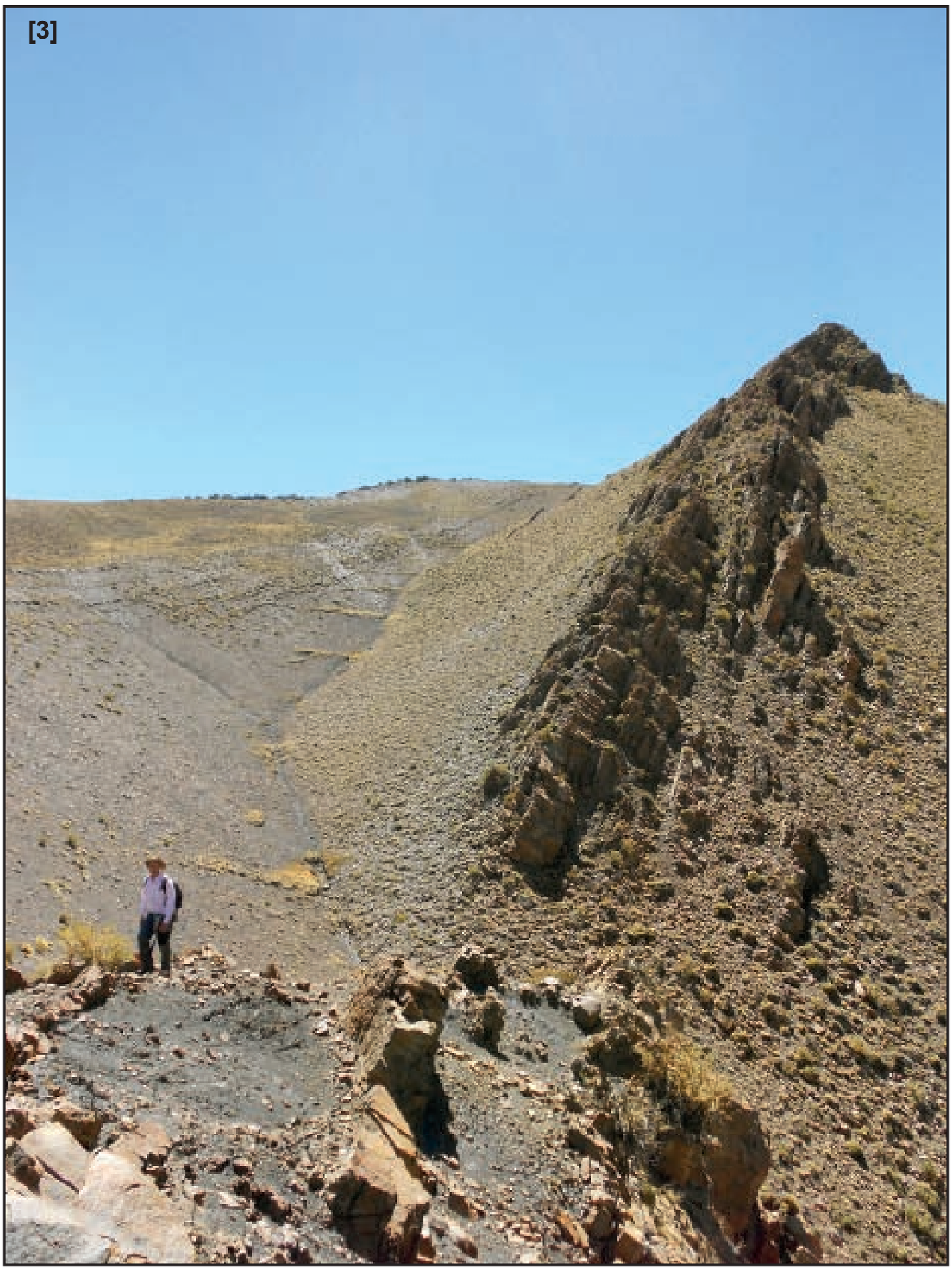

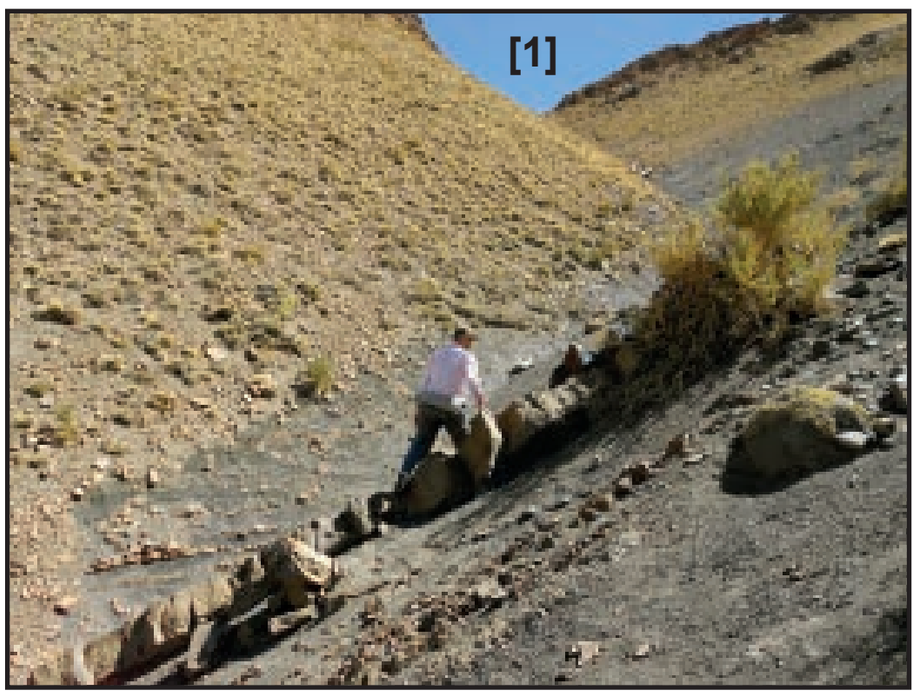

SUPPLEMENTARY FIGURE 2-D

Triassic–Jurassic boundary section at Arroyo Alumbre:
34°49’767’’S – 69°53’224’’W (Google-maps coordinates: -34.827675, -69.888884)

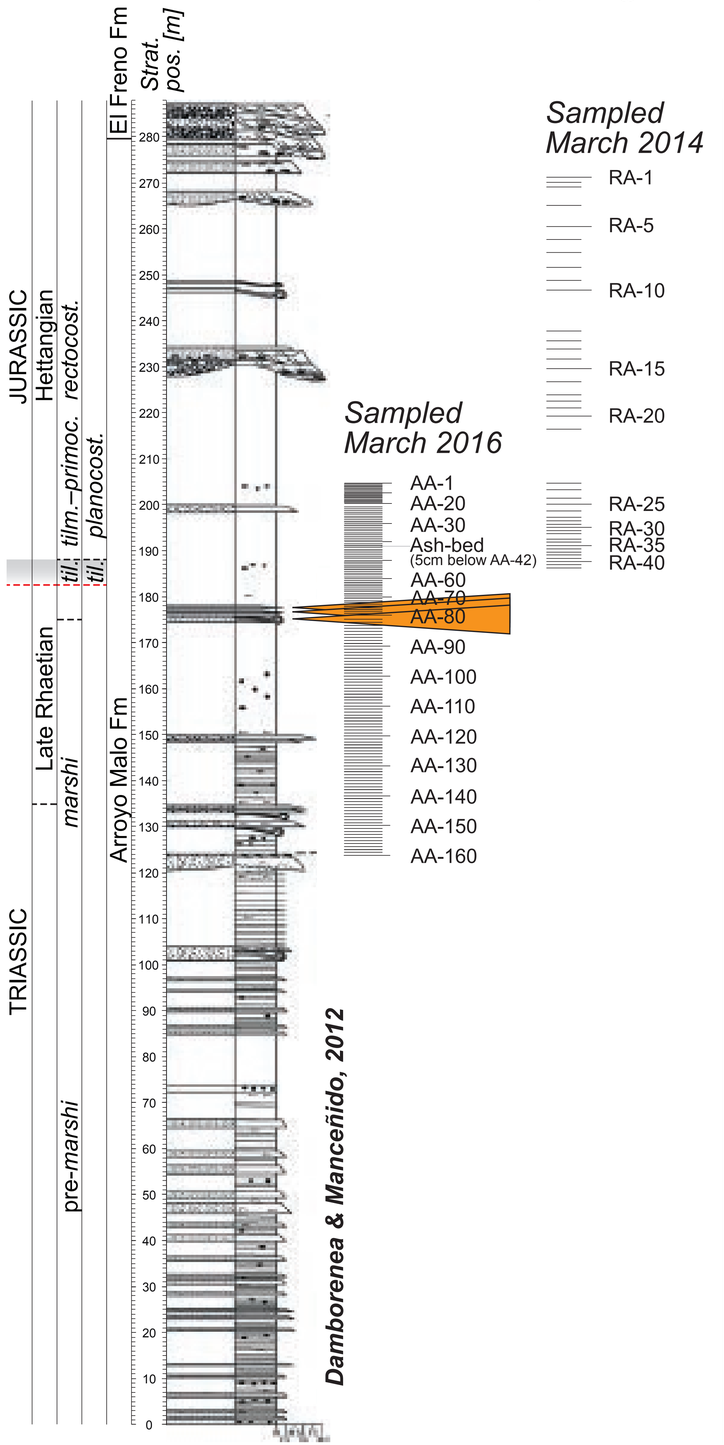

SUPPLEMENTARY FIGURE 2-E

Triassic–Jurassic boundary section at Arroyo Alumbre:
34°49’767”S – 69°53’224”W (Google-maps coordinates: -34.827675, -69.888884)

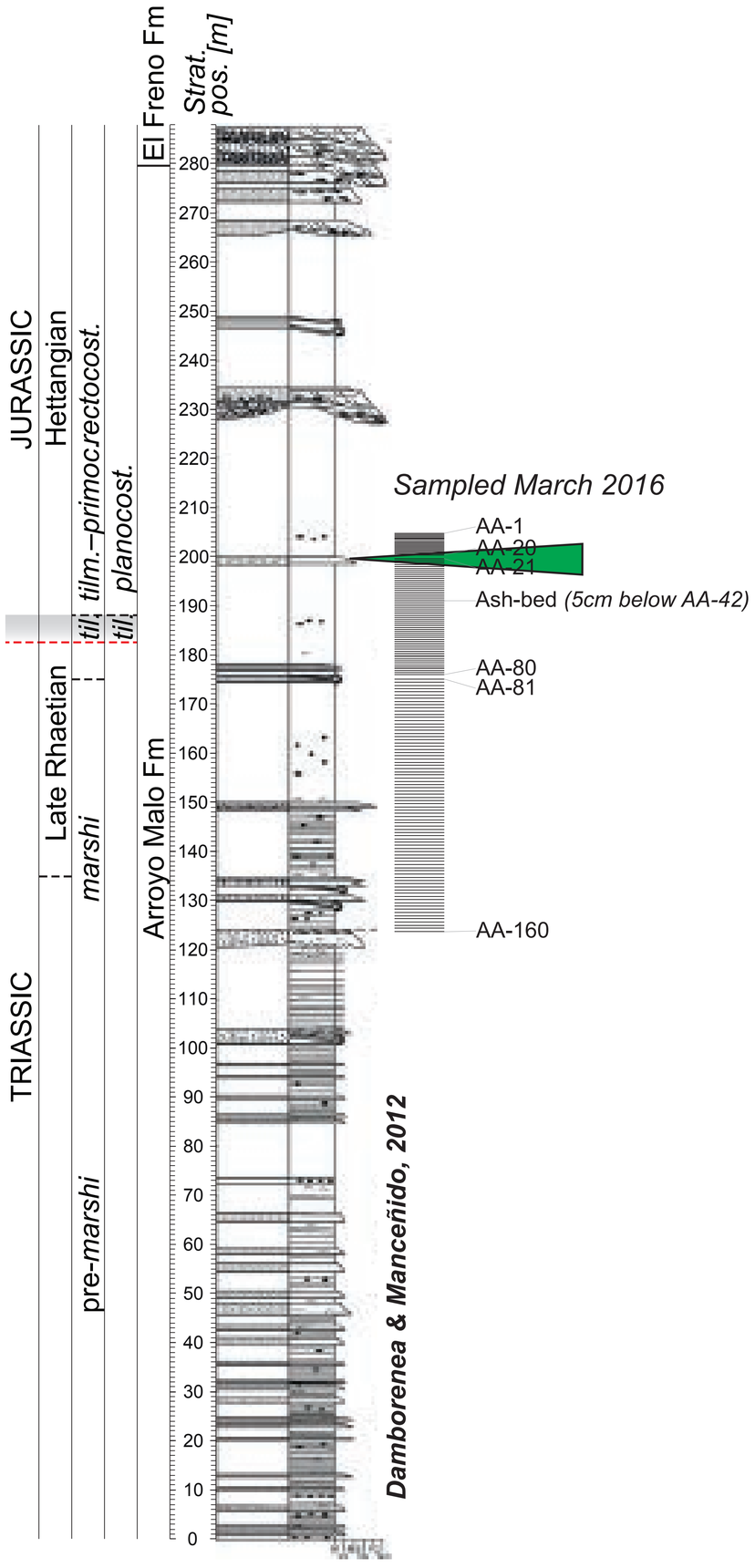

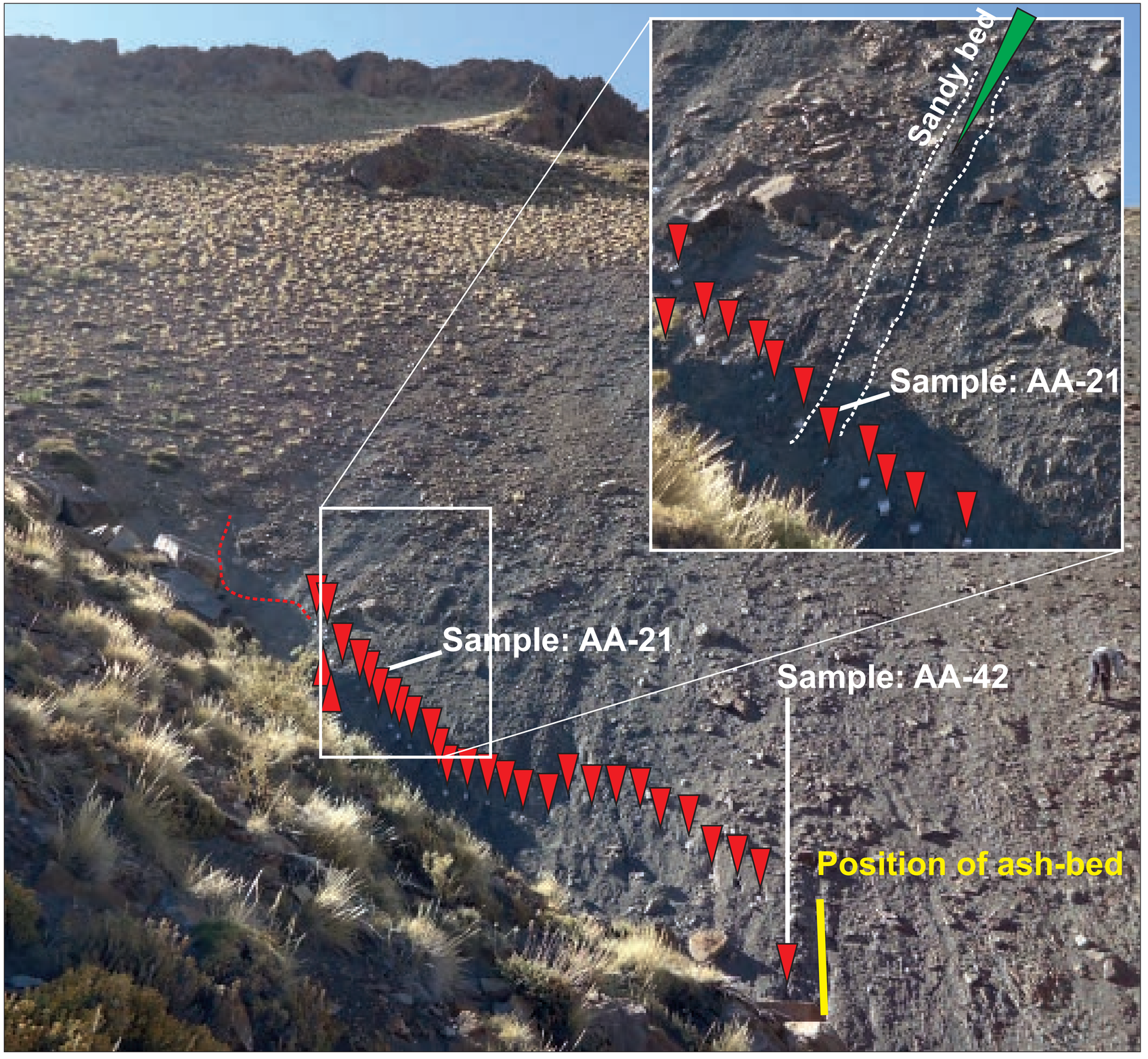

SUPPLEMENTARY FIGURE 3